Molecular Mechanisms of Cellular Mechanosensing

Tianzhi Luo, Krithika Mohan, Pablo A. Iglesias, and Douglas N. Robinson

Supplementary Materials

Supplementary Materials includes Supplementary Text, Supplementary Tables 1-5, Supplementary Figures 1-20, and Supplementary Movies S1-S9.

Supplementary Text

The force-sharing between actin cytoskeletal proteins during cell deformation

A popular structural model for cells assumes that they have a mostly elastic cortical shell, consisting of the actin cortex and plasma membrane, encapsulating the largely viscous cytoplasm (with organelles). During deformation, the actin cortex bears external loads while the plasma membrane mainly provides the resistance to bending deformation [1, 2]. Besides myosin II and actin, other load-bearing elements include the actin crosslinkers (ACs) and force-transmitting anchoring proteins (**Supplementary Fig. 1b**). The ACs organize individual actin filaments into structures such as bundles and meshwork [3, 4], whose relative abundance is determined, in part, by the relative concentrations of two classes of ACs [5]. Anchoring proteins then bridge the actin cortex to the plasma membrane. Finally, the mechanical properties of the actin cortex depend on the force-dependent affinities of all of these proteins for F-actin and their concentrations [6, 7]. Two kinds of experimental evidence support this idea. First, the deletion or depletion of different ACs reduced the cortical tension to different degrees as compared to that of WT cells (**Supplementary Fig. 1c**). Additionally, depletion of ACs in *myoII* null cells further reduced cortical tension as compared to *myoII* null alone [8]. Second, the viscoelastic moduli of both cells and artificially assembled actin gels measured by particle tracking methods increased with higher concentrations of ACs across a wide force range [3, 6-9]. To further illustrate how force is transmitted and shared at the cellular level, it is useful to recognize the relationships between the proteins in the cytoskeleton-membrane composite (**Supplementary Fig. 5)**. Myosin II and actin crosslinkers act somewhat in parallel with each other as they constitute the cortical network, which acts in series with the anchoring proteins that link the meshwork to the plasma membrane.

Superposition of the contribution of cytoskeleton proteins to the mechanical properties of cells

The localization of the actin cytoskeletal proteins was assessed using live cell imaging of cells expressing FP-fusion proteins (**Supplementary Fig. 1a; Supplementary Table 1**). These proteins are enriched in the actin cortex next to the plasma membrane but depleted in the cytoplasm. The Young's modulus or the stiffness of the cells is the summation of the contributions from all cytoskeletal proteins, and the reduction of any cytoskeletal protein concentration generally leads to reduced cell stiffness. Cortical tension measured by micropipette aspiration is usually considered an equivalent physical parameter of the cell. A schematic graph of the molecular structure of an aspirated cell is shown in **Supplementary Fig. 1b**. The reduction of cortical tension compared to WT cells due to the deletion of

myosin II and ACs is shown in **Supplementary Fig. 1c**. Comparison of the cortical tension between WT and *myosin II* null indicates that myosin II contributes 10~20% to the cortical tension. In *racE* null cells, multiple ACs, such as coronin and dynacortin, are inactivated and the cortical tension is only 1/3 of that of WT cells.

Myosin II does not affect many cytoskeletal proteins in the micropipette

Importantly, myosin II did not have an effect on the mechanosensitive accumulation of many cytoskeletal proteins (**Fig. 2a; Supplementary Fig. 6**), including two anchoring proteins, myosin I (a PH-domain-containing protein) and enlazin (a FERM-domain-containing protein). The proteins involved in adhesion also did not show much accumulation, indicating that the so-called "inside-out" signaling found in focal adhesion proteins was not prominent at the cortex during micropipette aspiration. Although probes for actin, GFP-actin, LimEΔcoil, and Lifeact-mRFP, displayed transient accumulation in WT cells (**Supplementary Movie S2 and 3**), they did not show accumulation in *myosin II* null cells, implying that actin accumulation itself is not mechanosensitive. Actin's transient accumulation in WT cells is probably a result of waves that have been observed in various *Dictyostelium* mutants [10-12]. Other probes for the molecules that act upstream of actin polymerization, including cofilin, HSPC300 (a SCAR subunit), p41-Arc (an Arp2/3 complex subunit), small GTPases and regulators of phosphatidylinositol phosphates, similarly did not accumulate due to cortical deformation, and most were insensitive to the presence of myosin II (**Fig. 2a; Supplementary Fig. 6**). However, a few proteins such as cofilin appeared to be depleted from the cortex of *myoII* null cells in response to mechanical stress (**Fig. 2a; Supplementary Fig. 6**). Finally, a general transmembrane protein, the cAMP-receptor car1, also showed no force-induced accumulation (**Fig. 2a; Supplementary Fig. 6**).

Coarse-grained molecular mechanics model (Fig. 3a,b)

The cell membrane and the underlying actin cortex may be considered a membrane-cortex composite. The cell membrane, composed of a lipid bilayer, contributes to the bending rigidity [1] while the actin cortex, with a thickness ranging from a few hundred nanometers to one micron, dominates the in-plane stretch modulus of the composite. The cortical actin network includes actin, ACs, and myosin II.

The actin filaments are nearly undeformable when their lengths are below 500 nm [13]. Therefore, at low force regimes, most of the deformations occur at the binding interface between ACs and actin filaments although the ACs and myosin II themselves are deformable at relatively high force regimes.

From single molecule measurements, it is known that the binding of ACs and myosin II to actin filaments is force-dependent [14]: some binding life-times increase with force while others may decrease with force. Thus, the microstructures and corresponding mechanical properties of the membrane-cortex composite are mainly governed by the force-dependent binding affinities of actin binding proteins.

The whole membrane-cortex composite can be discretized into inter-connected triangle elements where the average length of sides of the triangles is an indicator of the mesh size of the actin cytoskeleton model (**Supplementary Fig. 8**). The nodes of these triangles represent the crosslinking positions and the triangles mimic the meshes in the actin network. As Discher *et al.* suggested [1, 2], the total Helmholtz free energy of the composite at the coarse-grained molecular level can be calculated by

$$E_{total} = E_{bending} + E_{in-plane} + E_{surface} + E_{volume}. \tag{S1}$$

The bending energy, $E_{bending}$, mainly contributed by the plasma membrane, is written as

$$E_{bending} = \tfrac{1}{2}\sum_{i,j} k_{bend}\left(1-\cos(\theta_i - \theta_i^0)\right), \tag{S2}$$

where k_{bend} is the bending modulus, $\theta_{i,j}$ is the angle between the surface normal to the elements *i* and *j*, and θ_i^0 is the reference value of θ_i at equilibrium. The in-plane free energy $E_{in-plane}$ has the form

$$E_{in-plane} = \sum_i V_{WLC}(l_i) + \tfrac{1}{2}\sum_i k_{dilation}(A_i - A_i^0)^2 . \tag{S3}$$

The first term $V_{WLC}(l_i)$ is the worm-like-chain energy due to the intermolecular and intramolecular deformations of actin cytoskeletal proteins associated with edge, l_i. The second term is the energy due to the dilation/shrinking of individual mesh of area A_i with initial value A_i^0 and a dilation modulus, $k_{dilation}$. Specifically, the force in the worm-like-chain model is

$$f_{WLC}(l) = -\frac{\partial V_{WLC}(l)}{\partial x} = -\frac{nk_BT}{p}\left(\frac{1}{4(1-x)^2} - \frac{1}{4} + x\right), \quad x = \frac{l}{l_{\max}} \in (0,1), \tag{S4}$$

where k_B is the Boltzmann constant, T is the temperature, $2n$ is the number of functional ACs between two connected nodes, $l_{\max}$ is the maximum length of edge l, and p is the average persistence length of the ACs. Here, the deformation of actin filaments is neglected because they are too rigid to deform since their length is much shorter (about 100 nm in *Dictyostelium* cells [8]) than their persistence length (~5 μm). $E_{surface}$ is the energy associated with the conservation of global surface area and is written as

$$E_{surface} = \tfrac{1}{2}k_{surface}(A_{total} - A_{total}^0)^2 , \tag{S5}$$

where $k_{surface}$ is the global area modulus, A_{total} is the total area of membrane-cortex composite and A_{total}^0 is the initial total area. Similarly, E_{volume} is the energy associated with the conservation of global volume and has the form of

$$E_{volume} = \tfrac{1}{2} k_{volume}(V_{total} - V_{total}^0)^2 , \tag{S6}$$

where k_{volume} is the global volume modulus and V_{total} and V_{total}^0 are the total volume of the cell and its corresponding equilibrium value, respectively. Note that there are two terms associated with area change. The area change term in **Eq. S3** comes from a local perspective, *i.e.*, short-range propagation of elastic deformation in individual mesh; in contrast, the area terms in **Eq. S5** come from a global perspective, namely, the long-range feedback of the deformation in the whole actin network.

We used a surface mesh with 10,000 nodes and 19,996 triangles representing a sphere of radius 5 μm (the size of a *Dictyostelium* cell). The resultant edges are, on average, 70 nm long, which is close the average length of F-actin in *Dictyostelium* cells [8]. For **Eq. S4**, the average persistence length of ACs is on the order of 40 nm as measured experimentally [15, 16]. The average number of ACs, *n*, is assumed to be one for the time being. The values of the remaining parameters are: k_{bend}=100 k_BT, θ_i^0=0, $k_{dilation}$ = 100 k_BT, $k_{surface}$ = 1000 k_BT, k_{volume} =1000 k_BT, which are similar to those used in other coarse-grained simulations for cells and actin networks [1, 2, 17].

The motion of the node at position $\vec{r}$ is described by the Brownian dynamics equation (or over-damped Langevin dynamics equation)

$$\varsigma M \frac{d\vec{r}}{dt} = -\frac{\partial \Delta E_{total}}{\partial \vec{r}} + \vec{f}_{external} + \vec{f}_{contractile} + \sqrt{2\varsigma M k_B T}\, R(t) , \tag{S7}$$

where ς is the damping coefficient, M is the mass, $\vec{f}_{external}$ is localized external force, $\vec{f}_{contractile}$ is the contractile force-dipole due to myosin II pulling, and $R(t)$ is zero-mean Gaussian noise. $R(t)$ satisfies $\langle R(t) \rangle = 0$ and $\langle R(t)R(t') \rangle = \delta(t-t')$ where $\delta(t)$ is the delta function. Here, the term ςM has the value of $6\pi\eta a$, where η is the viscosity of the cytoplasm, for which the relevant value is ~300 Pa•s for *Dictyostelium* cells [18, 19], a is the average size of the ACs, which is ~30 nm [20, 21], and $\vec{f}_{contractile}$ is a function of the local myosin II concentration.

The initial configuration of the system was obtained by thermal annealing at room temperature until the fluctuation of the system energy was less than 10^{-3}. This configuration was then mapped to an aspirated shape with the cell length in the pipette, L, equal to the desired values [1]. The final configuration of the system was achieved after 20 seconds of Brownian dynamics simulation with a 10^{-5} second time-step, according to **Eq. S7**. Meanwhile, $\vec{f}_{contractile}$ was set to 0 since the experimentally observed local accumulation of myosin II did not happen in this moment and the isotropic coarse-grained myosin contraction at basal level was already grouped into $k_{dilation}$. The 20-second simulation was long enough to relax the system to its equilibrium state.

The process described above was performed for three lengths of micropipette aspiration: L=2R_p, 3R_p, and 4R_p, where R_p is the radius of the micropipette. For each case, the area dilation of each node was calculated through averaging of the area dilation of the triangles with which the node of interest is associated. Similarly, the angle change of each node was determined. The area dilation and angle change along the axis of symmetry of the pipette (**Supplementary Fig. 8b**, **c)** were evaluated by averaging the corresponding values of the nodes that have the same coordinate on the axis. The contour plots of the deformations on the cell surface (**Supplementary Fig. 8d, e**) were created using the software Tecplot (www.tecplot.com). The maximum dilation deformation occurred in the tip region while the maximum shear deformation was in the neck region of the aspirated cells.

The deformation fields for compressed cells were calculated in a similar manner after the triangle mesh was mapped to a pancake shape while maintaining volume conservation. Unlike the micropipette case, for a compressed cell, the maximum dilation and the maximum shear almost coincided with each other while the dilation deformation had a sharper gradient (**Supplementary Fig. 11a**).

Myosin II is sensitive to dilation deformation

The functional unit of myosin II is the bipolar thick filament (BTF) (**Supplementary Fig. 12**). In *Dictyostelium* cells, BTFs are typically ~200-400 nm in length [22, 23]. Myosin II heads extend out from the two opposite ends and bind to actin filaments with opposite orientations. Using the energy from ATP hydrolysis, myosin heads pull the actin filament towards its plus end. Myosin II pulling is most effective when the motors interact with two anchored antiparallel actin filaments, which conversely lock the motor heads in their isomeric state, increasing their binding lifetimes on F-actin. Any deviations from antiparallel orientation reduce the mechanical power generated by the myosin II heads [24] and therefore the increase of binding lifetimes is reduced.

During dilation deformation, the distance between two adjacent crosslinking points in the actin network increases through displacement between two nearby antiparallel actin filaments. This displacement raises the tension along the actin filaments, helps the motor heads to be locked and thus enhances their F-actin binding affinities. On the other hand, shear deformation associated with the angle change between actin filaments does not promote locking of the motor heads in the isomeric state and therefore leads to a smaller effect on the actin-binding affinity of myosin II. Therefore, myosin II is mostly sensitive to dilation, which is provided by the displacement of two antiparallel actin filaments (**Fig. 3e; Fig. 4c**).

In cells, the BTFs undergo constant assembly and disassembly. This turnover dynamics can be described by a force-dependent myosin II BTF assembly/disassembly scheme that is able to quantitatively account for the accumulation of local myosin II at the cellular level (**Supplementary Fig. 12** and Ref. [25]). This model was used to account for the two lines in Fig. 1d corresponding to different values of ζ. In the first case, all the applied stress (ζ=1) was used to simulate myosin II accumulation. In the second case, only one seventh of the applied stress (ζ =1/7) was used to calculate the corresponding myosin II accumulation, which was lower.

Model of force-dependent crosslinking mechanism of dimerized α-actinin in response to dilation (Fig. 3d,f)

The functional unit of some ACs, such as α-actinin, is a dimer, and the two ends of the dimer have equivalent actin binding domains. The binding of the dimers can be visualized as a two-step process that is sensitive to dilation (**Supplementary Fig. 12a, b**). In the first step, one end of the freely diffusing AC dimer binds to an actin filament in a nearby region while the other end still moves freely without binding to anything. Once the first step finishes, the AC dimer and the actin filament form a complex whose diffusivity is much reduced (as compared to the freely diffusing unattached AC) due to tethering of the AC to the actin network. Consequently, fast motion of the other end is restricted to a 3D sphere whose radius is determined by the length of the dimer. In the second step, the free end of the dimer searches for an available actin filament in this spherical volume and binds to it. Similarly, the diffusivity of the final complex consisting one AC dimer and two actin filaments is also very small. This two-step binding reaction can be written as $[Cr]+[F_1]\leftrightarrow[CrF_1]+[F_2]\leftrightarrow[CrF_1F_2]$, where Cr, F_1 and F_2 represent the crosslinker, the actin filament in step one and the actin filament in step two, respectively, and square brackets denote concentrations. The reaction-diffusion equations corresponding to this binding reaction are

$$\begin{aligned}
\frac{\partial[Cr]}{\partial t} &= D_1\nabla^2[Cr] - (k_{on_1}[Cr][F_1] - k_{off_1}[CrF_1]) \\
\frac{\partial[CrF_1]}{\partial t} &= D_2\nabla^2[CrF_1] + (k_{on_1}[Cr][F_1] - k_{off_1}[CrF_1]) - (k_{on_2}[CrF_1][F_2] - k_{off_2}[CrF_1F_2]), \\
\frac{\partial[CrF_1F_2]}{\partial t} &= D_3\nabla^2[CrF_1F_2] + (k_{on_2}[CrF_1][F_2] - k_{off_2}[CrF_1F_2]),
\end{aligned} \tag{S8}$$

where D_1, D_2 and D_3 are the diffusion coefficients of *Cr*, CrF_1 and CrF_1F_2, respectively. The Stokes-Einstein equation was used to calculate D_1 based on the viscosity of *Dictyostelium* cytoplasm and the size of monomeric α-actinin [20]. Since D_2 and D_3 are intrinsically associated with tethered diffusion due to the connectivity of actin network, their values are much smaller than those calculated by the Stokes-Einstein equation. The parameters k_{on_i} and k_{off_i} (i=1,2) are the on- and off-rates, respectively. The above partial differential equations obey mass conservation over the complete cell:

$$\int[Cr_{total}]dV = \int([Cr] + [CrF_1] + [CrF_1F_2])dV \tag{S9}$$

because there is no protein exchange between cells and the culture media, nor is there any net production/degradation of proteins in the time window of the experiments. Note, however, that at any point in the cell, the total concentration of the crosslinker can vary over time. In our model, $[F_1]$ is the F-actin concentration in the cytoplasm, which is ~72 μM [25]. $[F_2]$ is the effective concentration of actin filament binding sites in the spherical volume accessible to the AC dimers. This sphere size is defined by the length of the rod-like α-actinin dimer, which is ~30 nm. If one actin filament is found in this volume the local actin concentration of filaments (not actin monomers in the filament form) is ~5 μM. We assumed that each α-actinin can reach ~2 possible binding sites on the actin filament, raising the effective concentration to ~8-10 μM. Significantly, sensitivity analysis (not shown) confirmed that this is the effective concentration range for which simulations recapitulate the experimental data.

To account for the observed accumulations of α-actinin during micropipette aspiration, we considered several bond-types, including 1) force-independent bond, 2) slip-bond, 3) catch-bond, 4) structural cooperativity due to force-induced local reorganization of actin filaments, and 5) catch-slip transition.

For the different force-dependent behaviors, we assumed that k_{off_2} is the only force-dependent parameter since the AC dimers can feel the force in the actin network only when both ends are bound to F-actin. Although k_{on_2} could, in principle, also be force-dependent, there is no reported experimental evidence to support this. More specifically, this force-dependency has the form of $k_{off_2} = k_{off_2}^0 \exp(-f\Delta x/k_BT)$, where $k_{off_2}^0$ is zero-force off-rate, f is the force applied on the AC dimer

and Δx is the phenomenological bond length in a Bell-type model [26]. Based on the strain field calculation from the coarse-grained simulation (**Fig. 3a**; **Supplementary Fig. 8**), we assumed the force f changes gradually as a function of the azimuth angle θ. The simulation results based on simple catch-bond produce an accumulation pattern that is in good agreement with the experimental observation (**Supplementary Fig. 13d; Fig. 3d**). The simulations based on different bond models (catch-bond, slip-bond and force-independent bond) suggest that the catch-bond, but not force-independent or slip-bond, model is able to reproduce the accumulation kinetics measured experimentally (**Supplementary Fig. 13e; Fig. 3g**). Sensitivity analysis of k_{on_2} narrowed down the range of its value for the catch-bond model (**Supplementary Fig. 13f**). Different forces from 40 to 100 pN do not affect the accumulation significantly (**Supplementary Fig. 13g**).

In considering structural cooperativity, we hypothesized that in response to force, neighboring parallel actin filaments undergo translation and rotation such that the distance between these filaments favors more efficient binding of α-actinin thereby affecting the on-rate. More specifically, $k_{on_2} = k_{on_2}^0 \left(1 + [CrF_1F_2]/[F_2]\right)^{\chi \cos\theta}$, where θ is the azimuth angle in the tip region. In the absence of force-dependent mechanisms, the structural cooperativity in the region of the cell experiencing dilation is sufficient to generate local accumulation of α-actinin, reproducing the experimental observations (**Supplementary Fig. 14**). However, at a molecular level, it is unclear how dilation strain, but not shear strain, would lead to the structural cooperativity.

Finally, the catch-slip transition is a more complete model that covers multiple force-dependent behaviors. In this model, we adopt the formula proposed by Pereverzev *et al*. [27-29]:

$$k_{off_2} = k_{off_2}^{c0} \exp\left(-f\Delta x_c / k_B T\right) + k_{off_2}^{s0} \exp\left(-f\Delta x_s / k_B T\right), \qquad \text{(S10)}$$

where the superscripts and subscripts *c* and *s* represent the catch-bond and slip-bond, respectively. Here, the values for the catch-bond pathway ($k_{off_2}^{c0}$ and Δx_c) remain the same as in the simple catch-bond model. The values for the slip-bond pathway ($k_{off_2}^{s0}$ and Δx_s) are calculated from the ratios $k_{off_2}^{s0}/k_{off_2}^{c0}$ and $\Delta x_s/\Delta x_c$ used for muscle myosin II [28] or L/P selectin [27]. **Equation S10** allows k_{off_2} to increase with the force *f* in the low force regime and decrease in high force regime (**Supplementary Fig. 15a**). The simulated accumulation of α-actinin in the force range of 0 to 100 pN also displayed a rise-fall transition (**Supplementary Fig. 15b**). The maximum accumulation occurred at $f \approx 50$ pN where the kinetics using the ratios from muscle myosin II resembled more closely the experimental observations

(**Supplementary Fig. 15c**)**.** Nevertheless, the catch-slip transition model is more general than the catch and slip models alone.

In summary, both the catch-bond and the structural cooperativity models were able to reproduce the experimentally observed accumulation of α-actinin in the micropipette. However, the molecular basis for which dilation, but not shear deformation, would induce structural cooperativity is not clear. The catch-slip transition model is a more general treatment that accounts for larger force ranges.

Force-dependent crosslinking mechanism of dimerized filamin in response to shear (Fig. 3d,g)

The kinetics of filamin accumulation measured experimentally (**Fig. 3g**; **Supplementary Fig. 10**) show two important features: 1) a flat initial stage lasting for about 5 seconds; followed by 2) continuous acceleration afterwards. Since the hyperbolic kinetics observed in the binding mechanism of α-actinin are different from those of filamin, the binding mechanism of filamin must also be different from those of α-actinin (**Fig. 2c**; **Fig. 3f, g**; **Supplementary Fig. 10**). Moreover, the accelerated accumulation seen indicates the possibility of cooperativity.

Like α-actinin, filamin also forms dimers and undergoes two-step binding reactions during crosslinking (**Supplementary Fig. 16a**). However, unlike the parallel actin bundles crosslinked by α-actinin, filamin forms an actin meshwork in which the orientation of two crosslinked actin filaments may be at non-zero angles. In the absence of shear deformation, the four angles associated with one crosslinking point of two crosslinked actin filaments are about 90^o due to the four-fold rotational symmetry. After shearing, two angles become larger and two become smaller (the corresponding binding sites are defined as α and β sites, respectively; **Supplementary Fig. 16b**). Based on single molecule measurements [14], the different angles at α and β sites are expected to lead to different off-rates for filamin from F-actin. These two different binding affinities only exist when the two filamin monomers within a dimer are bound to F-actin at the same time, *i.e.*, in the second step of binding reactions (**Supplementary Fig. 16a**). Otherwise, the filamin dimer does not feel the force and force-induced affinity change does not occur. Using Cr, F_1 and F_2 to represent the crosslinker, the actin filament in the first step and the actin filament in the second step, respectively, the corresponding reaction-diffusion equations for filamin are written as

$$
\begin{aligned}
\frac{\partial[Cr]}{\partial t} &= D_1\nabla^2[Cr] - (k_{on_1}[Cr][F_1] - k_{off_1}[CrF_1]) \\
\frac{\partial[CrF_1]}{\partial t} &= D_2\nabla^2[CrF_1] + (k_{on_1}[Cr][F_1] - k_{off_1}[CrF_1]) - (k_{on_2}[CrF_1][F_2] - k^{\alpha}_{off_2}[Cr^{\alpha}F_1F_2]) \\
&\quad - (k_{on_2}[CrF_1][F_2] - k^{\beta}_{off_2}[Cr^{\beta}F_1F_2]) \qquad \text{(S11)} \\
\frac{\partial[Cr^{\alpha}F_1F_2]}{\partial t} &= D_3\nabla^2[Cr^{\alpha}F_1F_2] + (k_{on_2}[CrF_1][F_2] - k^{\alpha}_{off_2}[Cr^{\alpha}F_1F_2]) \\
\frac{\partial[Cr^{\beta}F_1F_2]}{\partial t} &= D_3\nabla^2[Cr^{\beta}F_1F_2] + (k_{on_2}[CrF_1][F_2] - k^{\beta}_{off_2}[Cr^{\beta}F_1F_2]).
\end{aligned}
$$

As above, D_1, D_2 and D_3 are the diffusion coefficients of *Cr*, CrF_1 and CrF_1F_2, respectively, and k_{on_i} and k_{off_i} (i=1,2) are the on- and off-rates, respectively. The Stokes-Einstein equation was again used to calculate D_1 based on the viscosity of *Dictyostelium* cytoplasm and the size of filamin [21]. D_2 and D_3 are assumed to be smaller than D_1 because they are intrinsically associated with tethered diffusion due to the connectivity of actin network. Here, $[F_1]$ is ~72 μM. The effective concentration $[F_2]$ is ~6 μM since the length of a filamin is ~25 nm, based on similar assumptions for $[F_2]$ as described for α-actinin (above).

Once again, we considered a number of cases to account for the observed accumulations of filamin in response to shear strain: 1) force-independent bond, 2) slip-bond, 3) catch-bond; 4) catch-bond mechanism plus the structural cooperativity due to force-induced local reorganization of actin filaments; and 5) catch-slip transition plus the structural cooperativity.

For different force-dependent behaviors, again we used the form $k_{off_2} = k^0_{off_2}\exp\left(-f\Delta x/k_BT\right)$. The values of the parameters can be found in **Supplementary Table 3**. After applying a force-profile in the tip region with catch-bond assumption, we observed a hyperbolic curve for filamin accumulation (**Supplementary Fig. 16e**) that is different from the experimental observations. This indicates that catch-bond alone does not give rise to the accelerated accumulation found in the experiments. Simulations of slip-bond and force-independent models failed to display any accumulation (not shown). Based on the binding kinetics of myosin II and cofilin to F-actin in *in vitro* assays [30, 31], it is known that accelerated binding usually comes from cooperative interactions at the molecular level.

For the fourth case, in addition to the Bell-type catch-bond formula for k_{off_2}, we incorporated structural cooperativity into k_{on_2}:

$$
k_{on_2} = k^0_{on_2}\left(1 + \frac{[Cr^{\alpha}F_1F_2] + [Cr^{\beta}F_1F_2]}{[F_2]}\right)^{\chi\cos\theta}, \qquad \text{(S12)}
$$

where $k_{on_2}^0$ is the on-rate of the second step without cooperativity, χ is the cooperativity index and θ is the azimuth angle in the tip region (**Supplementary Fig. 16c**). The rationale for the cooperativity is that when a CrF_1F_2 complex forms, it creates two non-parallel actin filaments with four V-shape binding sites for filamins (illustrated in **Supplementary Fig. 16a**). These four V-shape binding sites may allow more than four filamins to bind simultaneously because filamin dimers at the same binding site may stagger themselves with small relative displacements while maintaining their V-shape. Therefore, the formation of one CrF_1F_2 complex may promote more filamin molecules to bind the same junction of two actin filaments, F_1 and F_2. As a result, CrF_1F_2 complex inherently has cooperativity in the on-rate of filamin, k_{on_2}, during the crosslinking process. We proposed that the structural cooperativity is proportional to the local concentration of total CrF_1F_2 and the difference of on-rates between α and β sites may be neglected for simplification. Additionally, this cooperativity is limited by the local F-actin concentration, F_2, which leads to the normalization factor $[F_2]$. The cooperativity index χ possibly has direct physical implications on the local structures of filamin binding to F-actin [32]. χ=0 corresponds to the case of no cooperativity. The exact value of χ can be determined by comparing the kinetics of the simulated accumulations to the experimental observations. **Equation S12** is, of course, not the only form for cooperativity in k_{on_2}, and other possible forms could also work. Nevertheless, the cooperative forms should have three properties: (1) When there is no cooperativity (*i.e.*, χ=0), $k_{on_2}=k_{on_2}^0$ must be satisfied; (2) k_{on_2} is a power function of the concentration of crosslinked *Cr*, (*i.e.*, $[Cr^{\alpha}F_1F_2]+[Cr^{\beta}F_1F_2]$); and (3) cooperativity is limited by the local effective concentration of actin filaments (*i.e.*, $[F_2]$). Taking the structural difference between α and β sites into account, we further suggest that the terms for $k_{off_2}^{i}=k_{off_2}^0\exp\left(-f^i\Delta x/k_BT\right)$ for i=(α, β) have $\Delta x^{\alpha}>0$ and $\Delta x^{\beta}<0$. Mass conservation was maintained as described by **Eq. S9**. The values of the parameters may be found in **Supplementary Table 3**.

As shown in **Supplementary Fig. 16f,** the cooperativity index χ was determined by sensitivity analysis when both structural cooperativity and catch-bond were considered**.** If a difference of k_{off_2} exists for α and β sites, the agreement between simulation and experiment improves (**Supplementary Fig. 16g**). However, the model of structural cooperativity alone did not produce filamin accumulation kinetics observed experimentally (**Supplementary Table 3; Supplementary Fig. 16h**).

For the catch-slip transition model, we used **Eq. S10** where $k_{off_2}^{c0}$ and Δx_c had the same values as in the catch-bond. The values for $k_{off_2}^{s0}$ and Δx_s were calculated from the ratios of $k_{off_2}^{s0}/k_{off_2}^{c0}$ and $\Delta x_s/\Delta x_c$ assessed for muscle myosin II [28] and L/P selectin [27]. We also include the difference between α and β sites. The exact values of all the parameters are listed in **Supplementary Table 3**. Simulations showing the resulting k_{off_2} values at α and β sites for 0-120 pN are provided (**Supplementary Fig. 17a, b).** The simulated accumulation of filamin in this force range displayed an increase-decrease transition with the peak located at about 90 pN (**Supplementary Fig. 17c**). The kinetics of accumulation at *f*=90 pN indicate that the ratios of $k_{off_2}^{s0}/k_{off_2}^{c0}$ and $\Delta x_s/\Delta x_c$ used for muscle myosin II are suitable for filamin (**Supplementary Fig. 17d**).

Overall, to reproduce the experimentally-observed filamin accumulation in the micropipette, a minimal model must consider both catch-bond and structural cooperativity. By themselves, neither model reproduced the experimental observations. The catch-slip transition model is a more complete treatment that accounts for broader force ranges, including those not accessible in these experiments presented here.

Estimate of the molecular forces during cellular deformation

The applied pressure in this study is on the order of 1 nN/μm^2, and the cellular extension in the pipette is around a few μm. However, the physiological force on each protein is usually smaller than 100 pN and the maximum extension of each protein is usually a few tens of nm. To use the molecular mechanisms to quantitatively interpret the force-induced protein accumulation at the cellular level, it is necessary to link the cellular forces and deformations to those that individual proteins experience at the molecular level.

In experiments, the cell length L in the pipette increases up to 10 μm, equivalent to $4R_p$. Based on the deformations calculated by the coarse-grained molecular mechanics model, the area change corresponding to $L=4R_p$ is about 100% in the tip region of deformed cells, *i.e.*, the area dilation is about two fold. This results in an edge-stretch ratio $l/l_0 = (l_0 + \Delta l)/l_0 = \sqrt{2}$, where l_0 is the initial edge length and Δl is the change of the edge length. If l_0 is 70 nm, then the resulting deformation, Δl, is ~30 nm. On the other hand, when $L=4R_p$, the angle change associated with the shear deformation in the neck region of deformed cells is $\Delta\theta = (\Delta\theta/\theta_0)\times\theta_0 = 0.5\times 90^\circ = 45^\circ$.

The deformation at the molecular level is attributed to both inter-molecular and intra-molecular displacements. The inter-molecular deformation occurs at the interface between the actin-binding domains of proteins and F-actin. Based on single molecule deformations, the rupture forces for the actin-binding domains of mammalian filamin A and α-actinin are about 60 pN and 40 pN, respectively [14]. Since their counterparts in *Dictyostelium* cells share the same actin-binding domains, these values presumably may be applied to *Dictyostelium* filamin and α-actinin. The intra-molecular deformations include unfolding of protein domains and extension of flexible regions. The unfolding of one spectrin domain in α-actinin requires a force of 30 pN and gives rise to a corresponding extension of 32 nm [15]. This extension is close to the edge length change, Δl, calculated above using the coarse-grained molecular mechanics model. The unfolding of one Ig domains in filamin requires a force of 50 pN and gives rise to a corresponding extension of 17 nm [16]. This extension is also close to the edge length change, Δl. Additionally, the intra-molecular deformations can also occur by rigid rotation between domains in the same molecule, for example, the rotation between the two monomers within the same filamin dimer. Since the half-length of the *Dictyostelium* filamin dimer is ~25 nm, the end-to-end distance change of filamin is around +10.8 nm at α sites and is close to −16.2 nm at β sites when the angles have a change, $\Delta\theta$, of 45˚ with respect to its initial angle 90˚. The force associated with angle change is usually a product of the bending modulus of the molecule and the angle change value. So far, there has been no measured value for the bending modulus of a filamin dimer. Therefore, the reported values are based on either estimation or simulations: the bending moduli being used in some computational research are in the range of 100 to 1000 k_BT [17, 33], which leads to a force of a few hundred pN. In contrast, molecular dynamics simulations from other researchers also demonstrated that a pair of forces about 5 pN at the two ends of *Dictyostelium* filamin is large enough to cause significant angle change [33].

Based on the published values [14] and the above discussion, we used 40 pN and 60 pN for the parameter f in the Bell-type off-rates for α-actinin (**Supplementary Table 2)** and filamin (**Supplementary Table 3)**, respectively, to account for the force-dependency in their binding affinities. These forces roughly result in 10-fold changes in k_{off_2}. Nevertheless, the simulations with catch-slip transition **(Supplementary Tables 2, 3; Supplementary Figs. 15, 17**) provide insight into how the accumulations change over a wider force range.

Simulation of the accumulations of cytoskeletal proteins (Fig. 1d, 3d-g)

The accumulation of myosin II, α-actinin and filamin were simulated by solving the corresponding reaction-diffusion equations in a 3D-aspirated cell shape using COMSOL Multiphysics (Burlington, MA) (**Supplementary Fig. 13-17**). In the simulations, the cell diameter is 10 μm, and the pipette radius is 2.5 μm. The reaction-diffusion equations for myosin II are based on the BTF assembly scheme of myosin II, which was described in detail previously [25]. The reaction-diffusion equations for α-actinin and filamin are listed above in **Eq. S8** and **Eq. S11**, respectively, and the corresponding values of the parameters are summarized in **Supplementary Tables 2 and 3**. The input force-profiles for dilation and shear strains are based on the coarse-grained simulations (**Fig. 3a**; **Supplementary Fig. 8**), and the estimations of molecular force are described in the previous sections. The force-profile for dilation sensitivity is $f_{\max}\sin\theta$ where θ defines the azimuth angle in the tip region, and $f_{\max}$ is 40 pN for α-actinin (**Supplementary Fig. 13c**). The force-profile for shear sensitivity is $f_{\max}\cos\theta$ for the tip region and $f_{\max}$ for the neck region (**Supplementary Fig. 16c**). $f_{\max}$ is 60 pN for filamin. Reasonable values of k_{on_2} for both α-actinin and filamin were found by sensitivity analysis to identify the values that provided good agreement between simulations and experiments (**Supplementary Fig. 13f**; **Supplementary Fig. 16f**). The measured diffusion coefficient of α-actinin in solution is ~30 μm^2/s [34]. Considering the diffusion coefficient of GFP is 3-fold slower in *Dictyostelium* cells than that in solution [35], we set the cellular diffusion coefficient of α-actinin to be 10 μm^2/s. When the CrF_1 and CrF_1F_2 complexes are tethered to the cortical actin network, their diffusion must be much slower than that of free α-actinin. Here, we assumed that $D_2 = D_3 = D_1/50$ for α-actinin. Considering the size difference between α-actinin and filamin, we used D_1 = 5.0 μm^2/s, $D_2 = D_1/100$, and $D_3 = D_1/1000$ for filamin. Outside the cortical region, we set $D_1 = D_2 = D_3$. The simulation results of α-actinin and filamin for different mechanisms are provided (**Fig. 3**; **Supplementary Fig. 13-17**).

Model for cell retraction due to accumulations of cytoskeletal proteins in the tip region (Fig. 4a,b)

The cytoskeleton-membrane composite is a viscoelastic material. In general, we describe this using a one-dimensional viscoelastic model (**Supplementary Fig. 19a**) consisting of a Voigt element (with elastic spring constant k_1 and viscosity η_1 in parallel) in series with a Maxwell element (with elastic spring constant k_2 and viscosity η_2 in series), in which case the position of the tip is given by:

$$L(t) = L(0) + \frac{1}{\eta_1}\int_0^t e^{-(k_1/\eta_1)(t-\tau)}\sigma_{\text{total}}(\tau)\mathrm{d}\tau + \frac{1}{k_2}\sigma_{\text{total}}(t) + \frac{1}{\eta_2}\int_0^t \sigma_{\text{total}}(\tau)\mathrm{d}\tau, \qquad \text{(S13)}$$

where σ_{total} is the stress acting on the viscoelastic material. To obtain the length of cell inside the pipette requires the parameters of the viscoelastic model (k_1, η_1, k_2, η_2) as well as the total stress acting on the cell.

The viscoelastic parameters can be obtained during creep tests, in which a constant aspiration stress is applied at time 0. In this time scale, $\sigma_{total} = P_{app}$, for $t \geqq 0$ and the length simplifies to:

$$L(t) = L(0^-) + P_{app}\left[\frac{1}{k_1}\left(1 - \exp\left(-k_1 t / \eta_1\right)\right) + \frac{1}{k_2}\left(1 + \frac{k_2}{\eta_2} t\right)\right], \tag{S14}$$

where $L(0^-)$ is the length immediately preceding the application of the aspiration pressure. The four parameters can be determined by fitting experimental data to this equation. For example, measurements of k_2 and η_2 are straightforward since the instantaneous cell length immediately after application of the aspiration pressure is $L(0^+) = L(0^-) + P_{app}/k_2$, and the elongation rate at long time scale is $\dot{L}(\infty) = P_{app}/\eta_2$. For *filamin* null and *α-actinin* null cells, these parameters were sufficient to fit the creep data, suggesting that the Voigt model is unnecessary in these strains (equivalently, that η_1/k_1 is negligible). For *racE* null cells, however, the characteristic time $\tau = \eta_1/k_1$ is on the order of a few seconds, and hence cannot be ignored. These were obtained by least squares minimization between measured and simulated trajectories (**Supplementary Table 4**).

Our experiments and simulations of cell retraction (**Fig. 4a,b** and **Supplementary Fig. S18**) take place over a considerably longer time scale (~100-250 s vs. 20-30 s) than the creep experiments. In this time scale, the viscous (η_2) properties dominate the elastic (k_2) component in the Maxwell model. Thus, the simulations for the *filamin* null, *α-actinin* null and *dynacortin-hp* cells use the model

$$L(t) \approx L(0) + \frac{1}{\eta_2}\int_0^t \sigma_{total}(\tau)\mathrm{d}\tau . \tag{S15}$$

For *racE* null cells, the elastic-Voigt model obtained in the creep experiments is appropriate.

For the cell retraction simulations, we also require a measure of the total stress acting on the cell:

$$\sigma_{total} = P_{app} - \sigma_{myo} - \sigma_{cross} + \sigma_{ten} . \tag{S16}$$

The four components on the right-hand side refer to the applied pressure from the micropipette, the stress exerted by the accumulated myosin and cross-linkers, and the cortical tension outside the pipette, respectively. The cortical tension measurements show that the contribution of the membrane is much smaller and hence is neglected in this study (**Supplementary Fig. 1c**).

To compute the contractile pressure due to accumulated myosin, we take the fluorescence intensity measured at the tip, $I_{myo}(t)$, and normalize this for volume using a factor (I_0=0.82) determined empirically by measuring soluble GFP [36]. We multiply this ratio by the concentration of myosin II in the cell (3.4 μM [37]) and use this as the concentration of myosin II at the aspirated tip. This value is then converted into a stress. To this end we take this concentration and compute the number of myosin II molecules per unit area by multiplying by the thickness of the cortex, assumed to be 0.5 μm and by Avogadro's number (N_A). We multiply this by the fraction of myosin II in BTF form (k_{BTF}; between 20-60%, as reported previously [38]), and by two to account for the number of heads in a myosin II motor. Finally, we multiply by the force per head (4 pN) [39, 40], and by the duty ratio (within 10-fold of its zero-force value; *i.e.*, between 0.006 and 0.06 [37]). Thus, a measured intensity $I_{myo}(t)$ is converted to a contractile stress according to the following formula:

$$\sigma_{myo} = (I_{myo} / I_0) \times (3.4\mu\text{M}) \times (0.5\mu\text{m}) \times 2k_{BTF} \times N_A \times (\text{duty ratio}) \times (\text{force / head}). \quad \text{(S17)}$$

Note that this stress is contractile and thus works against the applied micropipette pressure, hence the negative sign in Equation S16 above.

To compute the passive pressures due to the accumulation of the active crosslinkers, we use the formula for Laplace pressure: $\sigma_{cross}=2\gamma_{cross}/R_p$, where R_p is the radius of the pipette (assumed to be 2 μm). As observed in experiments, ACs, such as cortexillin I, α-actinin, and dynacortin, exhibit different levels of accumulation in the tip region over time. We define:

$$\gamma_{cross}(t) = \gamma^0_{cross} + \Delta\gamma(I_{cross}(t) / I_0 - 1). \quad \text{(S18)}$$

The term γ^0_{cross} is the crosslinker contribution in the absence of force, Δγ is the change of cortical tension due to accumulation of crosslinkers (assumed to be 0.3 nN/μm based on cortexillin I's contribution to cortical tension since cortexillin I accumulates along with myosin II [36]), and $I_{cross}(t)$ is the fluorescence intensity of accumulated crosslinkers.

Finally, we include the passive cortical tension (at the other end of the cell): $\sigma_{ten} = 2\gamma^0_{cross} / R_c$, where R_c is the radius of the cell outside the pipette (assumed to be 5.0 μm). Parameter values used for *filamin* null, *α-actinin* null, *dynacortin-hp* and *racE* null cells are listed in **Supplementary Table 5**.

It is worth pointing out that the retractions we studied are due to myosin II accumulation, unlike the ones associated with blebbing [41], which is the process of the rupture and healing of the linkages between actin cortex and plasma membrane. In comparison to the study of bleb-associated retractions

which uses a viscoelastic model similar to ours (**Eq. S15**) [42], we used measured myosin II signals rather than constant contractile stresses.

Supplementary References

1. Discher, D.E., Boal, D.H. & Boey, S.K. Simulations of the erythrocyte cytoskeleton at large deformation. II. Micropipette aspiration. *Biophys. J.* **75**, 1584-1597 (1998).
2. Li, J., Dao, M., Lim, C.T. & Suresh, S. Spectrin-level modeling of the cytoskeleton and optical tweezers stretching of the erythrocyte. *Biophys. J.* **88**, 3707-3719 (2005).
3. Wagner, B., Tharmann, R., Haase, I., Fischer, M. & Bausch, A.R. Cytoskeletal polymer networks: The molecular structure of cross-linkers determines macroscopic properties. *Proc. Natl. Acad. Sci. U. S. A.* **103**, 13974-13978 (2006).
4. Gardel, M.L. *et al.* Prestressed F-actin networks cross-linked by hinged filamins replicate mechanical properties of cells. *Proc. Natl. Acad. Sci. USA* **103**, 1762-1767 (2006).
5. Schmoller, K.M., Lieleg, O. & Bausch, A.R. Cross-linking molecules modify composite actin networks independently. *Phys. Rev. Lett.* **101**, 118102 (2008).
6. Shin, J.H., Gardel, M.L., Mahadevan, L., Matsudaira, P. & Weitz, D.A. Relating microstructure to rheology of a bundled and cross-linked F-actin network in vitro. *Proc. Natl. Acad. Sci. U. S. A.* **101**, 9636-9641 (2004).
7. Gardel, M.L. *et al.* Elastic behavior of cross-linked and bundled actin networks. *Science* **304**, 1301-1305 (2004).
8. Reichl, E.M. *et al.* Interactions between myosin and actin crosslinkers control cytokinesis contractility dynamics and mechanics. *Curr. Biol.* **18**, 471-480 (2008).
9. Girard, K.D., Chaney, C., Delannoy, M., Kuo, S.C. & Robinson, D.N. Dynacortin contributes to cortical viscoelasticity and helps define the shape changes of cytokinesis. *EMBO J.* **23**, 1536-1546 (2004).
10. Gerisch, G. *et al.* Mobile actin clusters and traveling waves in cells recovering from actin depolymerization. *Biophy. J.* **87**, 3493-3503 (2004).
11. Diez, S., Gerisch, G., Anderson, K., Müller-Taubenberger, A. & Bretschneider, T. Subsecond reorganization of the actin network in cell motility and chemotaxis. *Proc. Natl. Acad. Sci. U. S. A.* **102**, 7601-7606 (2005).
12. Taniguchi, D. *et al.* Phase geometries of two-dimensional excitable waves govern self-organized morphodynamics of amoeboid cells. *Proc. Natl. Acad. Sci. U. S. A.* (2013).
13. Palmer, J.S. & Boyce, M.C. Constitutive modeling of the stress/strain behavior of F-actin filament networks. *Acta Biomater.* **4**, 597-612 (2008).
14. Ferrer, J.M. *et al.* Measuring molecular rupture forces between single actin filaments and actin-binding proteins. *Proc. Natl. Acad. Sci. U. S. A.* **105**, 9221-9226 (2008).
15. Rief, M., Pascual, J., Saraste, M. & Gaub, H.E. Single molecule force spectroscopy of spectrin repeats: low unfolding forces in helix bundles. *J. Mol. Biol.* **286**, 553-561 (1999).
16. Schwaiger, I., Kardinal, A., Schleicher, M., Noegel, A.A. & Rief, M. A mechanical unfolding intermediate in an actin-crosslinking protein. *Nat. Struct. Mol. Biol.* **11**, 81-85 (2004).
17. Kim, T., Hwang, W., Lee, H. & Kamm, R.D. Computational analysis of viscoelastic properties of crosslinked actin networks. *PLoS Comput. Biol.* **5**, e1000439 (2009).
18. Feneberg, W., Westphal, M. & Sackmann, E. Dictyostelium cells' cytoplasm as an active viscoplastic body. *Eur. Biophys. J.* **30**, 284-294 (2001).
19. Zhang, W. & Robinson, D.N. Balance of actively generated contractile and resistive forces controls cytokinesis dynamics. *Proc. Natl. Acad. Sci. U. S. A.* **102**, 7186-7191 (2005).
20. Wachsstock, D.H., Schwarz, W.H. & Pollard, T.D. Affinity of α-actinin determines the structure and mechanical properties of actin filament gels. *Biophys. J.* **65**, 205-214 (1993).

21. Popowicz, G.M. *et al.* Molecular structure of the rod domain of Dictyostelium filamin. *J. Mol. Biol.* **342**, 1637-1646 (2004).
22. Mahajan, R.K. & Pardee, J.D. Assembly mechanism of *Dictyostelium* myosin II: Regulation by K^+, Mg^{2+}, and actin filaments. *Biochemistry* **35**, 15504-15514 (1996).
23. Mahajan, R.K., Vaughan, K.T., Johns, J.A. & Pardee, J.D. Actin filaments mediate Dictyostelium myosin assembly in vitro. *Proceedings of the National Academy of Sciences of the United States of America* **86**, 6161-6165 (1989).
24. Tanaka, H., Ishijima, A., Honda, M., Saito, K. & Yanagida, T. Orientation dependence of displacements by a single one-headed myosin relative to the actin filament. *Biophys. J.* **75**, 1886-1894 (1998).
25. Luo, T. *et al.* Understanding the cooperative interaction between myosin II and actin cross-linkers mediated by actin filaments during mechanosensation. *Biophys. J.* **102**, 238-247 (2012).
26. Bell, G.I. Models for the specific adhesion of cells to cells. *Science* **200**, 618-627 (1978).
27. Pereverzev, Y.V., Prezhdo, O.V., Forero, M., Sokurenko, E.V. & Thomas, W.E. The two-pathway model for the catch-slip transition in biological adhesion. *Biophys. J.* **89**, 1446-1454 (2005).
28. Guo, B. & Guilford, W.H. Mechanics of actomyosin bonds in different nucleotide states are tuned to muscle contraction. *Proc. Natl. Acad. Sci. U. S. A.* **103**, 9844-9849 (2006).
29. Luo, T. & Robinson, D. The role of the actin cytoskeleton in mechanosensation, in *Mechanosensitivity and Mechanotransduction*, Vol. 4. (eds. A. Kamkin & I. Kiseleva) 25-65 (Springer Netherlands, 2011).
30. Greene, L.E. & Eisenberg, E. Cooperative binding of myosin subfragment-1 to the actin-troponin-tropomyosin complex. *Proc. Natl. Acad. Sci. U.S.A.* **77**, 2616-2620 (1980).
31. De La Cruz, E.M. & Sept, D. The kinetics of cooperative cofilin binding reveals two states of the cofilin-actin filament. *Biophys. J.* **98**, 1893-1901 (2010).
32. Nakamura, F., Osborn, T.M., Hartemink, C.A., Hartwig, J.H. & Stossel, T.P. Structural basis of filamin A functions. *J. Cell. Biol.* **179**, 1011-1025 (2007).
33. Kolahi, K.S. & Mofrad, M.R.K. Molecular mechanics of filamin's rod domain. *Biophys. J.* **94**, 1075-1083 (2008).
34. Wachsstock, D.H., Schwarz, W.H. & Pollard, T.D. Cross-linker dynamics determine the mechanical properties of actin gels. *Biophys. J.* **66**, 801-809 (1994).
35. Potma, E.O. *et al.* Reduced protein diffusion rate by cytoskeleton in vegetative and polarized Dictyostelium cells. *Biophys. J.* **81**, 2010-2019 (2001).
36. Kee, Y.-S. *et al.* A mechanosensory system governs myosin II accumulation in dividing cells. *Mol. Biol. Cell* **23**, 1510-1523 (2012).
37. Robinson, D.N., Kee, Y.S., Luo, T. & Surcel, A. 7.5 Understanding how dividing cells change shape, in *Comprehensive Biophysics*. (ed. H.E. Edward) 48-72 (Elsevier, Amsterdam; 2012).
38. Zhou, Q. *et al.* 14-3-3 coordinates microtubules, rac, and myosin II to control cell mechanics and cytokinesis. *Curr. Biol.* **20**, 1881-1889 (2010).
39. Kovacs, M., Thirumurugan, K., Knight, P.J. & Sellers, J.R. Load-dependent mechanism of nonmuscle myosin 2. *Proc. Natl. Acad. Sci. U.S.A.* **104**, 9994-9999 (2007).
40. Veigel, C., Molloy, J.E., Schmitz, S. & Kendrick-Jones, J. Load-dependent kinetics of force production by smooth muscle myosin measured with optical tweezers. *Nat. Cell Biol.* **5**, 980-986 (2003).
41. Charras, G.T., Yarrow, J.C., Horton, M.A., Mahadevan, L. & Mitchison, T.J. Non-equilibration of hydrostatic pressure in blebbing cells. *Nature* **435**, 365-369 (2005).

42. Brugués, J. *et al.* Dynamical organization of the cytoskeletal cortex probed by micropipette aspiration. *Proc. Natl. Acad. Sci. U. S. A.* **107**, 15415-15420 (2010).
43. Goldmann, W.H. & Isenberg, G. Analysis of filamin and α-actinin binding to actin by the stopped flow method. *FEBS Lett.* **336**, 408-410 (1993).
44. Ren, Y. *et al.* Mechanosensing through cooperative interactions between myosin II and the actin crosslinker cortexillin I. *Curr. Biol.* **19**, 1421-1428 (2009).

Supplementary Table 1. List of proteins studied and the corresponding plasmids.

Protein	***Plasmid***
myosin II	GFP-myosin II-pDRH, GFP-myosin II-pBIG, mCherry-myosin II-pDRH
cortexillin I	mCherry-cortexillin I-pDM181
MHCKA	GFP-MHCKA-pTX
MHCKB	GFP-MHCKB-pTX
MHCKC	GFP-MHCKC-pTX
pakA	PakA-GFP-pMSG
PTEN	PTEN-GFP-pCV5
filamin	filamin-mRFP-pDXA
ACA	ACA-YFP-pCV5
PH-CRAC	PH-CRAC-GFP-pMSG
RBD	GFP-RBD-pDM323
PI3K2	PI3K2-GFP-pEXP4
actin	GFP-actin-pDM181
enlazin	GFP-enlazin-pLD1
fimbrin	fimbrin-GFP-pDRH, fimbrin-GFP-pLD1
dynacortin	GFP-dynacortin-pLD1
coronin	GFP-coronin-pLD1
α-actinin	GFP- α-actinin-pDN
ABP34	GFP-ABP34-pLD1
limE-Δ-coil	mCherry-limE-Δcoil-pDM181
Lifeact	Lifeact-mRFP-pDM181
p41-Arc	GFP-p41-Arc-pLD1
HSPC300	GFP-HSPC300-pDM459
cofilin	GFP-cofilin-pLD1
car1	mCherry-car1-pDM181
myosin IE	GFP-myosin IE-p1S1
myosin VII	GFP-myosin VII- pDTi112
rac1A	mCherry-rac1A-pDM181
racE	mCherry2-racE-pDM181
IQGAP2	GFP-IQGAP2-pEXP4
clcD	GFP-clcD-pDM181
14-3-3	14-3-3-GFP-pLD1
PP2A	YFP-PP2A-pTX
talin A	mCherry-talinA-pDXA
talin B	GFP-talinB-pDXA
sad A	sadA-GFP-pTX
paxillin B	GFP-paxB-pBIG

Supplementary Table 2. Parameters used in simulation of α-actinin dimer binding based on various assumptions.

Parameter	*Value*	*(units)*	*Resource*
Common Parameters			
$[F_1]$	72.0	μM	[37]
$[F_2]$	8.0	μM	estimated
D_1	10.0	$\mu m^2/s$	estimated (Stokes-Einstein)
$^{\#}D_2$	0.12-0.2	$\mu m^2/s$	estimated
$^{\#}D_3$	0.12-0.2	$\mu m^2/s$	estimated
k_{on_1}	1.1	$\mu M^{-1}s^{-1}$	[34]
k_{off_1}	5.2	s^{-1}	[34]
$k_{on_2}^0$	1.1	$\mu M^{-1}s^{-1}$	estimated
$k_{off_2}^0$	5.2	s^{-1}	[34]
Parameters for simulations using force-dependent mechanisms (Fig. 3d,f; Sup. Fig. 13d-g)			
f	40	pN	[14]
Δx (catch bond)	0.275	nm	[14]
Δx (slip bond)	−0.275	nm	[14]
Parameters for simulations using structural cooperativity with force-dependency (Sup. Fig. 14)			
χ	16		estimated
Parameters for simulations using catch-slip transition mechanism (Sup. Fig. 15)			
$k_{off_2}^{c0}$	5.2	s^{-1}	[34]
$^{*}k_{off_2}^{s0}$	0.42 1.09	s^{-1} s^{-1}	estimated based on muscle myosin II behavior estimated based on L/P selectin behavior
Δx_c	0.275	nm	[14]
$^{*}\Delta x_s$	−0.04 −0.03	nm nm	estimated based on muscle myosin II behavior estimated based on L/P selectin behavior

[#] Diffusion coefficients D_2 and D_3 apply to complexes formed in the cortex. For the comparable complexes in the cytoplasm, we let $D_1 = D_2 = D_3$.

[*] $k_{off_2}^{c0}$ and Δx_c are experimentally measured values [14, 34]. The values of $k_{off_2}^{s0}$ and Δx_s were calculated from the ratios $k_{off_2}^{s0} / k_{off_2}^{c0}$ and $\Delta x_s/\Delta x_c$ used for muscle myosin II [28] and L/P selectin [27].

Supplementary Table 3. Parameters used in simulation of filamin dimer binding based on various assumptions.

Parameter	*Value*	*(units)*	*Resource*
Common Parameters			
$[F_1]$	72.0	μM	[37]
$[F_2]$	6.0	μM	estimated
D_1	5.0	$\mu m^2/s$	estimated (Stokes-Einstein)
$^{\#}D_2$	0.05	$\mu m^2/s$	estimated
$^{\#}D_3$	0.005	$\mu m^2/s$	estimated
k_{on_1}	1.3	$\mu M^{-1}s^{-1}$	[43]
k_{off_1}	0.6	s^{-1}	[43]
$k^0_{on_2}$	0.01	$\mu M^{-1}s^{-1}$	estimated
$k^0_{off_2}$	0.6	s^{-1}	[43]
Parameters for simulations using force-dependency; no cooperativity (Fig. 3d,g; Sup. Fig. 16e)			
f^{α}	60	pN	[14]
f^{β}	60	pN	estimated
Δx (catch bond)	0.194	nm	[14]
Δx (slip bond)	−0.194	nm	[14]
Parameters for simulations using structural cooperativity (Sup. Fig. 16f-h)			
χ	9-13		estimated
Parameters for simulations using catch-slip transition mechanism (Sup. Fig. 17)			
$k^{c0}_{off_2}$ (α sites)	0.61	s^{-1}	[43]
$^{*}k^{s0}_{off_2}$ (α sites)	0.05 0.128	s^{-1} s^{-1}	estimated based on muscle myosin II behavior estimated based on L/P selectin behavior
Δx_c (α sites)	0.194	nm	[14]
$^{*}\Delta x_s$ (α sites)	−0.03 −0.02	nm nm	estimated based on muscle myosin II behavior estimated based on L/P selectin behavior
$k^{c0}_{off_2}$ (β sites)	0.05 0.128	s^{-1} s^{-1}	estimated based on muscle myosin II behavior estimated based on L/P selectin behavior
$^{*}k^{s0}_{off_2}$ (β sites)	0.61	s^{-1}	[43]
Δx_C (β sites)	0.03 0.02	nm nm	estimated based on muscle myosin II behavior estimated based on L/P selectin behavior
$^{*}\Delta x_s$ (β sites)	−0.03	nm	[14]

[#] Diffusion coefficients D_2 and D_3 apply to complexes formed in the cortex. For the comparable complexes in the cytoplasm, we let $D_1 = D_2 = D_3$.

[*] $k^{c0}_{off_2}$ and Δx_c had the values measured experimentally [14, 34]. The values of $k^{s0}_{off_2}$ and Δx_s were calculated from the ratios of $k^{s0}_{off_2}/k^{c0}_{off_2}$ and $\Delta x_s/\Delta x_c$ used for muscle myosin II [28] and L/P selectin [27].

Supplementary Table 4. Values of the viscoelastic parameters obtained by fitting creep tests (Supplementary Fig. 19) to Eq. S14.

	k_1 (nN/µm^3)	η_1 (nN•s/µm^3)	k_2 (nN/µm^3)	η_2 (nN•s/µm^3)
filamin null	N/A	N/A	0.35±0.05	39.7±6.0
α-actinin null	N/A	N/A	0.26±0.09	13.5±4.7
racE null	0.03±0.003	0.12±0.01	0.058±0.005	∞

Supplementary Table 5. Values of the parameters used in the simulations of cell retractions with Eqs. S15-S18.

	***force per myosin head* (pN)**	***duty ratio****	***BTF fraction*****	***Cortical thickness* (μm)**	η_2 **(nN•s/μm^3)**	***Applied pressure* (nN/μm^2)**
filamin null	4.0	0.06	50%	0.5	33.7	1.0
α-actinin null	4.0	0.06	30%	0.5	8.8	1.0
dynacortin-hp	4.0	0.06	20%	0.5	31.4	1.0
racE null	4.0	0.06	20%	0.5	5.0 (η_1)	0.4

* The duty ratio of *Dictyostelium* myosin II is about 0.006 at zero force, but may increase up to 10-fold with applied opposing force, resulting in force-dependent range of 0.006-0.06.

** The immobile fraction of *Dictyostelium* myosin II has an average of 40% with a range of ~20-60% in the cleavage furrow of a dividing cell (where the network is under mechanical stress) [38]. The immobile fraction appears to reflect the BTF fraction.

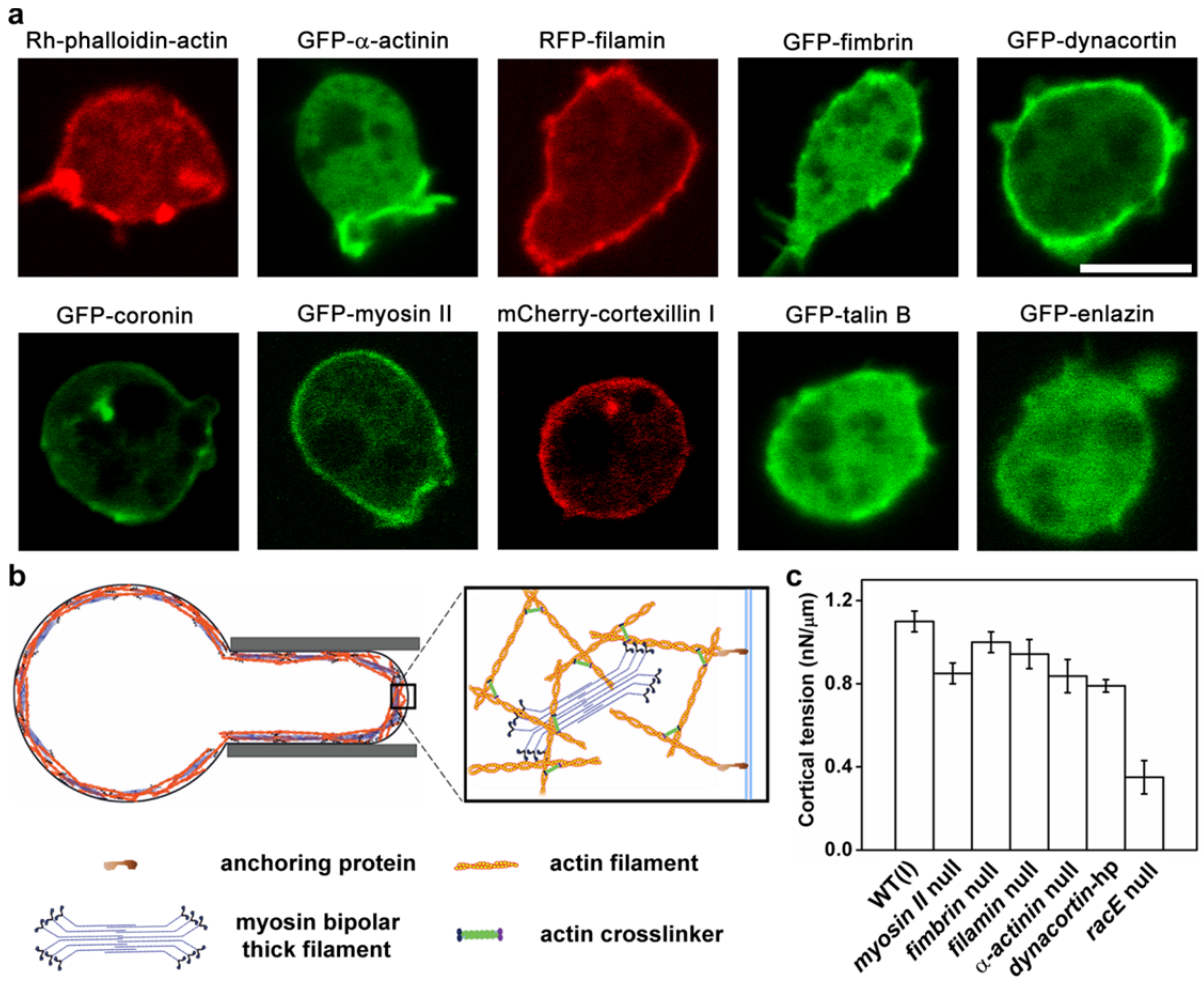

Supplementary Figure 1. The distribution of cytoskeletal proteins and the cortical tension of different mutants of *Dictyostelium*. **a**, The localization of ten cytoskeletal proteins taken by confocal microscopy. Scale bar, 10 μm. **b**, A schematic diagram of a cell aspirated by micropipette and the zoom-in of actin cortex and plasma membrane. **c**, The cortical tension of different mutants measured by micropipette aspiration. Except for *filamin* null and *α–actinin* null cells, the cortical tensions of other mutants were obtained from previous studies [8, 9].

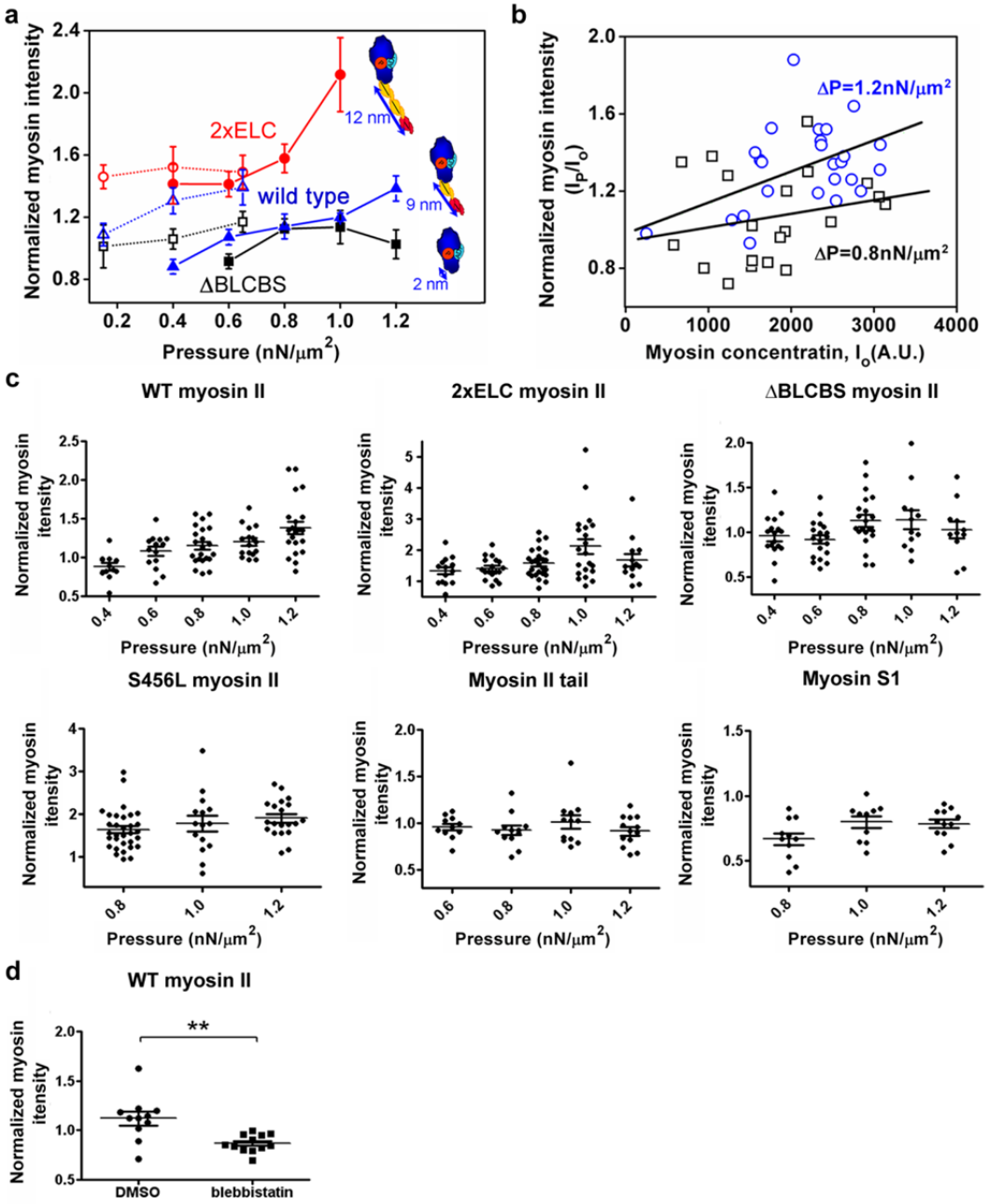

Supplementary Figure 2. The accumulation of different myosin II mutants at different pressures and the corresponding scatter plots. **a**, The accumulation of different myosin II mutants in mitosis (dotted lines) [44] and interphase (solid lines) at different pressures. **b**, Dependence of myosin II accumulation on its concentration at different pressures. **c**, The scatter plots of the myosin II accumulations. **d**, Blebbistatin (6 μM in 0.2% DMSO) inhibits myosin II accumulation. Asterisks (**) indicates the *p*-value <0.01, calculated using a Mann-Whitney test.

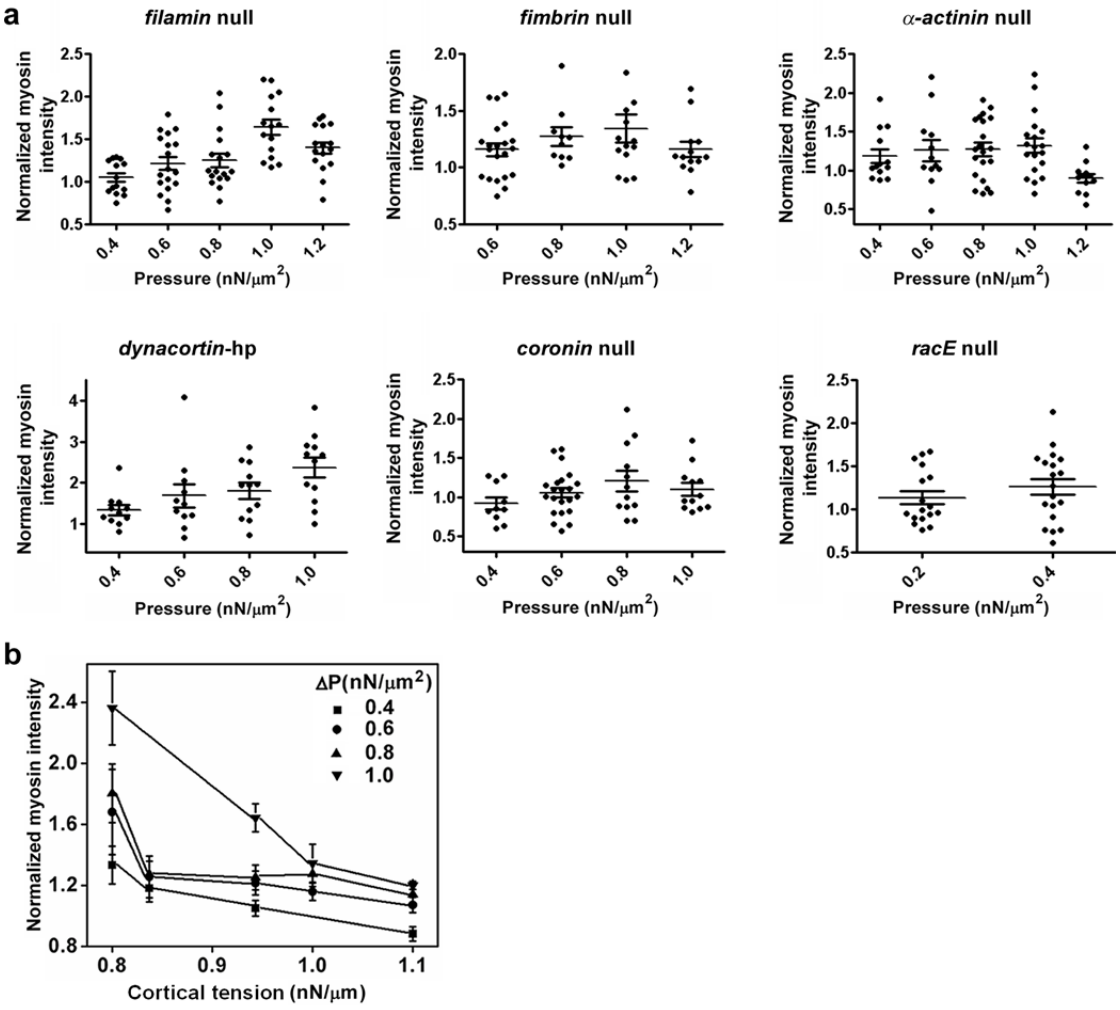

Supplementary Figure 3. The scatter plots of the accumulations of myosin II in different mutant cells and negative correlation between the cortical tension and myosin II accumulation. a, Myosin II accumulation in AC deletion mutants (*filamin* null, *fimbrin* null, *α-actinin* null, *dynacortin-hp*, *coronin* null and *racE* null) is higher than observed in WT cells in low and medium pressure region. But, myosin II accumulation levels decrease at high pressures possibly due to the rupture of the actin network with reduced connectivity, which impairs the force transmission to myosin II. **b**, Cortical tension and myosin II mechanosensitive accumulation are negatively correlated. Five strains tested here are WT, *filamin* null, *fimbrin* null, *α-actinin* null and *dynacortin-hp* (see **Supplementary Fig. 1c**), and the lines connect the accumulation values from the five stains measured at each pressure.

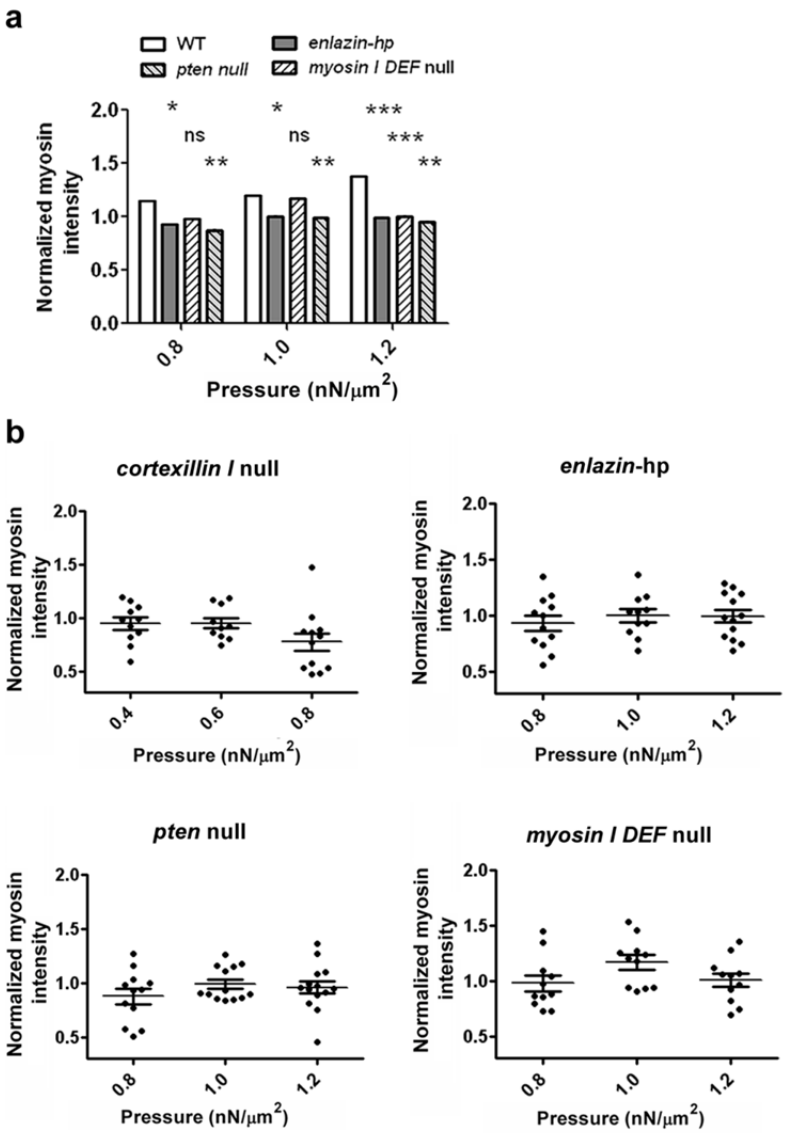

Supplementary Figure 4. Damage to the physical bridges between plasma membrane and actin cytoskeleton reduces myosin II accumulation. a, For simplicity, a bar graph of the means with the asterisks denoting statistical significance from a Mann-Whitney test is presented. Dot plots of composite data are in panel **b**, except for WT, which is shown in **Supplementary Fig. 2c**. **b**, Dot plots of all data for each strain and pressure are shown. Myosin II accumulation in the anchoring protein deletion mutants (*cortexillin I* null, *enlazin-hp*, *myosin I DEF* null and *pten* null) remained low across the entire pressure region.

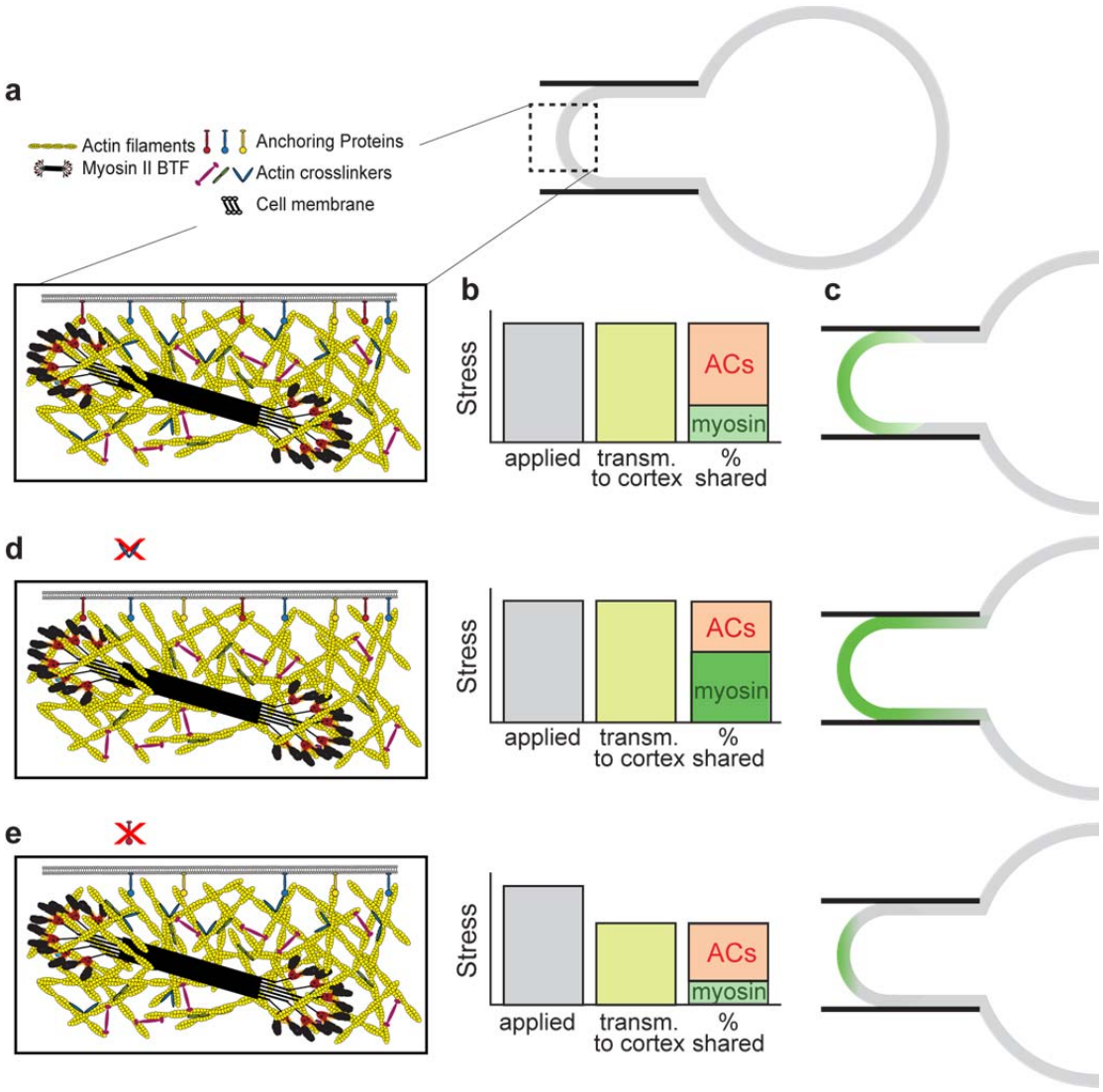

Supplementary Figure 5. Force sharing and the mechanosensory response. a, In this cartoon, force applied at the tip of the aspirated cell is transmitted through the membrane, membrane-anchoring and cortical (myosin II and crosslinkers) proteins. In this composite meshwork, the membrane-anchoring proteins act in series with the cortical proteins. **b,** Applied stresses (grey) must be transmitted through the membrane to the cortex (yellow) where they are shared by myosin II (green) and the other crosslinking proteins (red). **c,** This stress leads to a mechanosensory accumulation of myosin II at the tip. **d,** The effect of reducing/deleting some crosslinkers is to increase the amount of applied stress borne by myosin II, leading to greater accumulation at the tip. **e,** Reducing/deleting some of the anchoring proteins leads to lower accumulation, consistent with the view that the stress transmitted to the cortex is reduced. Further indicating a weakening in the membrane-cortex linkage, mutants deficient in anchoring proteins often form blebs at high applied pressures. Thus, the level of stress transmitted to the cortex is reduced, especially at these higher pressure regimes.

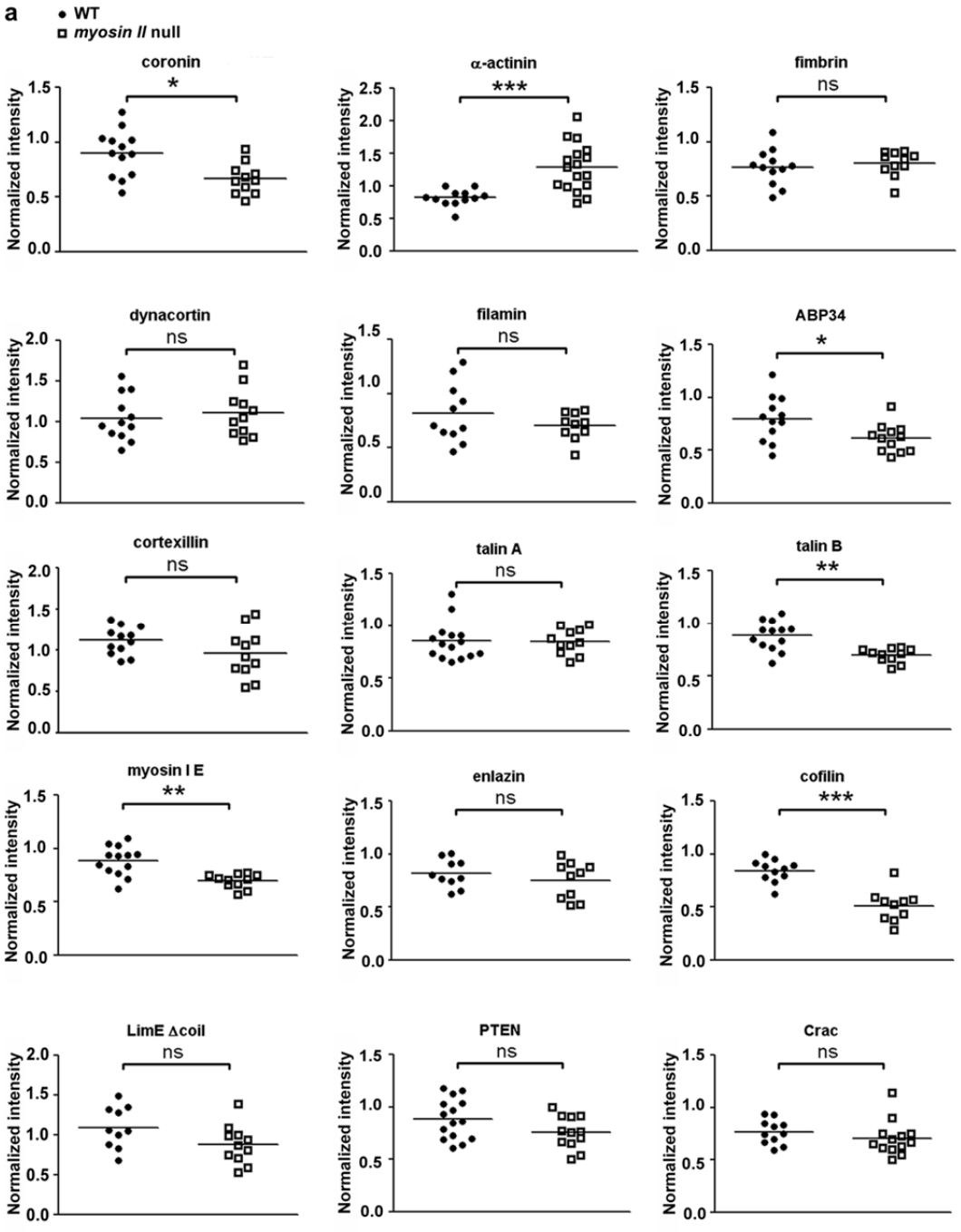

(Supplementary Figure 6; continued)

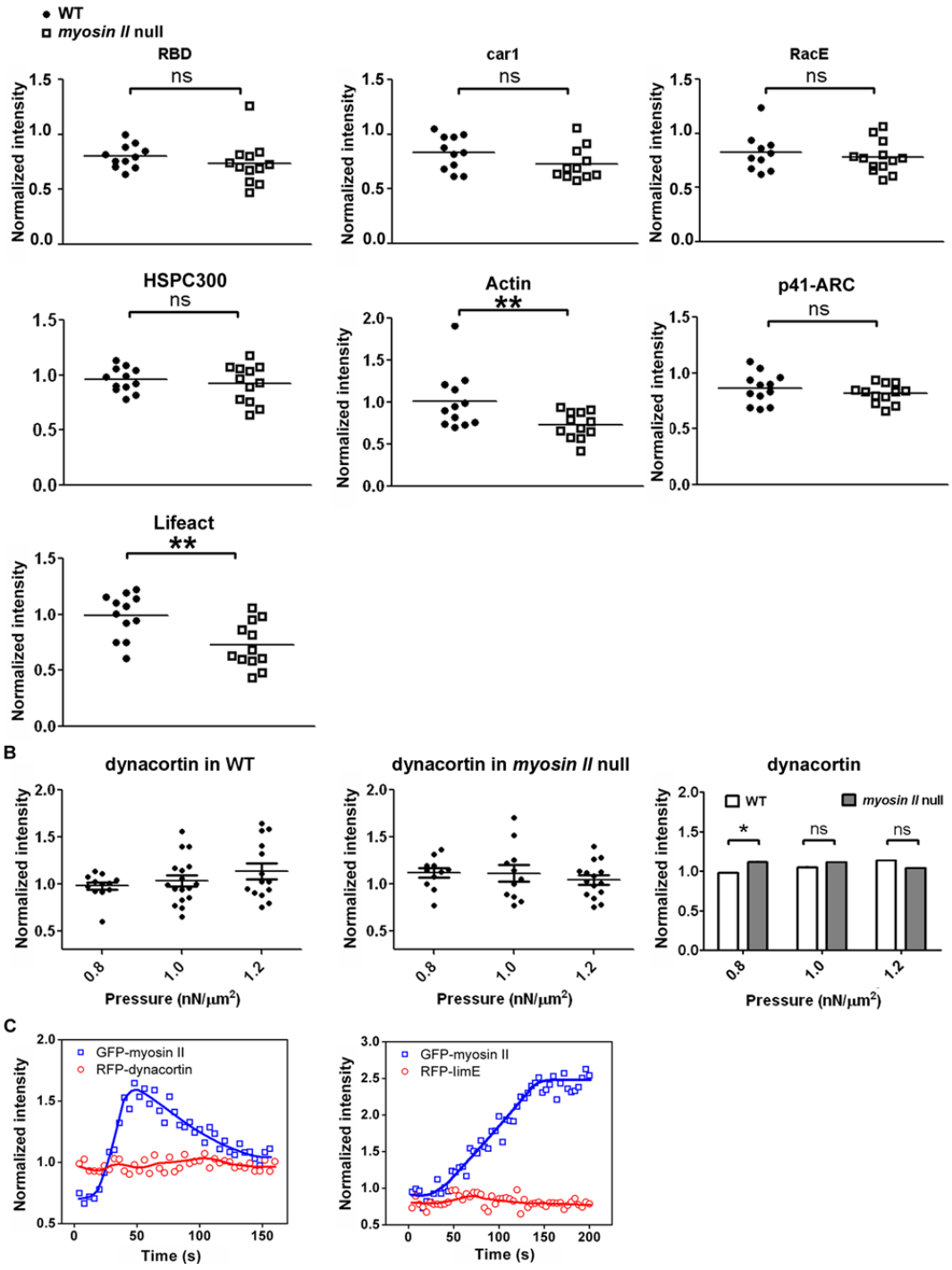

Supplementary Figure 6. Accumulation of cytoskeletal proteins in WT and *myosin II* null cells. a, Results of 18 proteins are shown for WT (filled circle) and *myosin II* null (open squares) cells at a pressure of 1.0 nN/μm^2. Panel **b**, shows data from three pressures for dynacortin accumulation in WT and *myosin II* null cells, respectively. **c**, Examples of the accumulation of dynacortin and limE-Δcoil. Asterisks *, ** and *** indicate *p*-values <0.05, <0.01, and <0.005, respectively, which were calculated using a Mann-Whitney test. Not significant is abbreviated "ns".

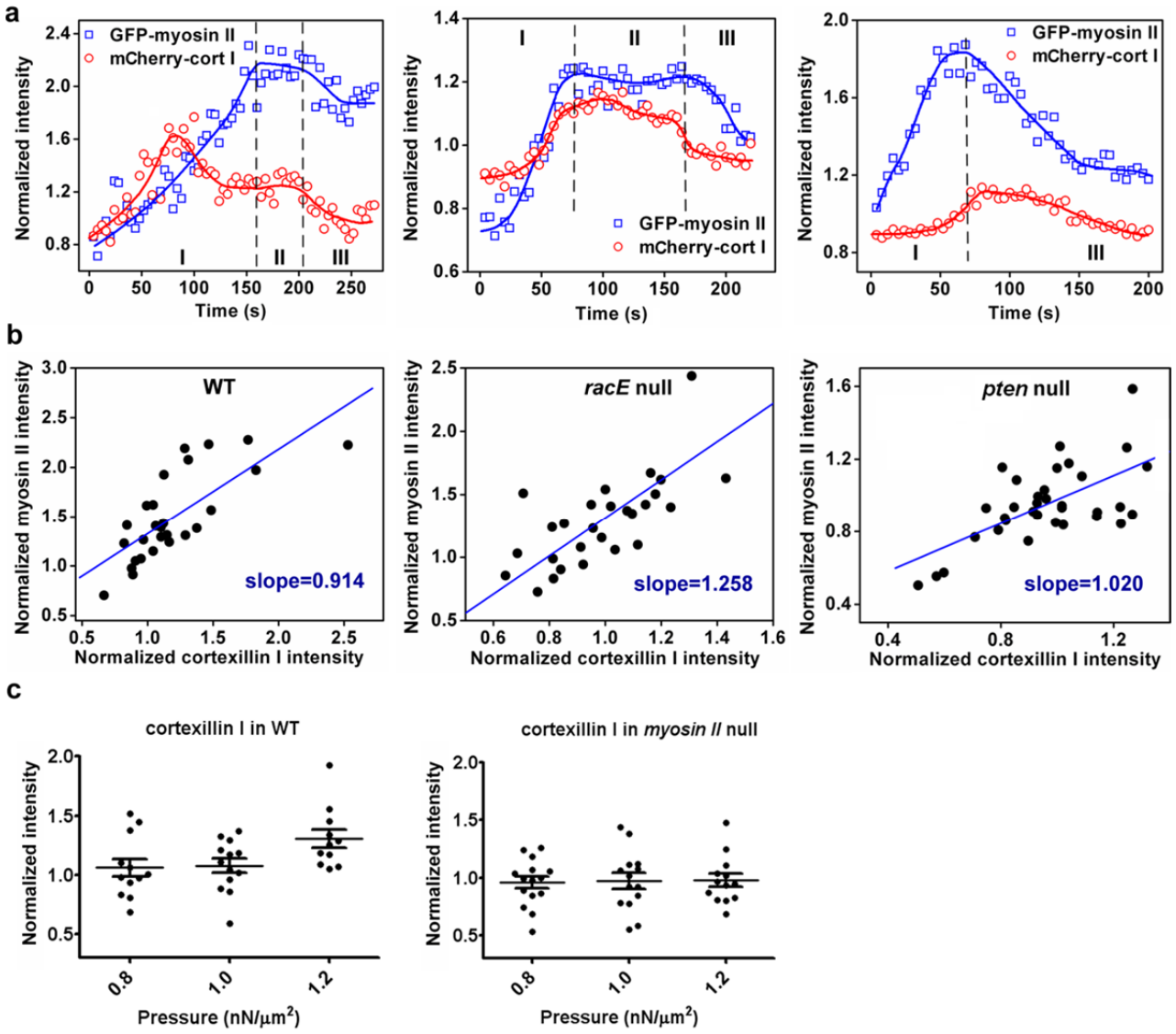

Supplementary Figure 7. Cooperative accumulation of myosin II and cortexillin I. **a**, Examples of the cooperative accumulation of myosin II and cortexillin I in WT cells. In general, the kinetics of the cooperative accumulation can be divided into three phases: (I) cooperative rise; (II) plateau; (III) cooperative decay. **b**, Correlations between the peak intensities of myosin II and cortexillin I accumulations in different mutants. Solid lines were fitted to the scattered data points. Measurements in a, and b, were conducted in cells co-expressing GFP-myosin II and mCherry-cortexillin I. **c**, The scatter plots of the cortexillin I accumulation in WT and *myosin II* null cells.

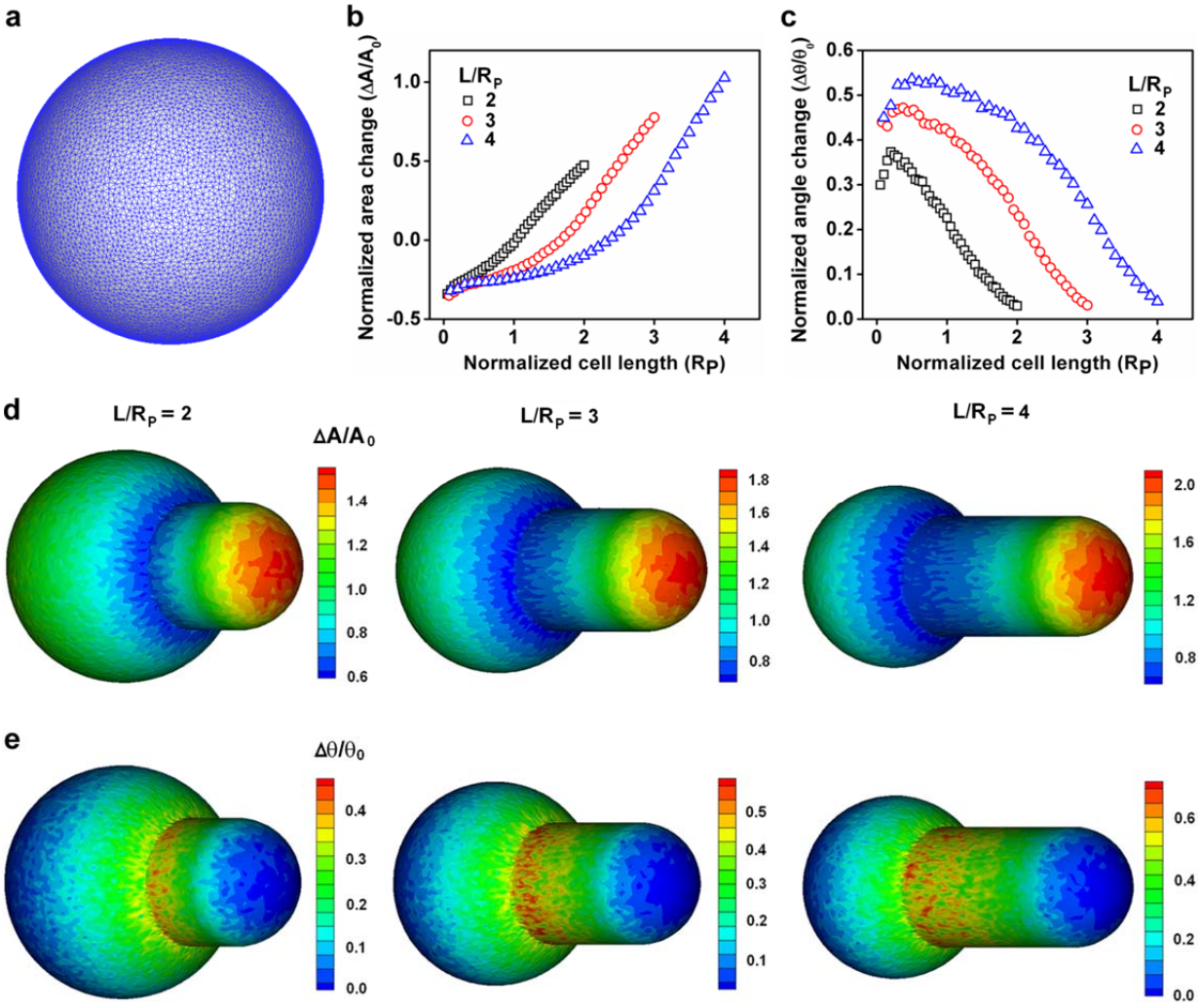

Supplementary Figure 8. The spatial profile of the deformation of actin cytoskeletal proteins calculated by the coarse-grained molecular mechanics model. **a**, The triangle mesh of the cytoskeleton-membrane composite. Panels **b**, and **c**, show the average dilation and shear strains over the rotation angle from the entrance of the pipette to the tip of cell for three different deformation states. Panels **d**, and **e**, show the corresponding detailed contour plots of the strains in each triangle element.

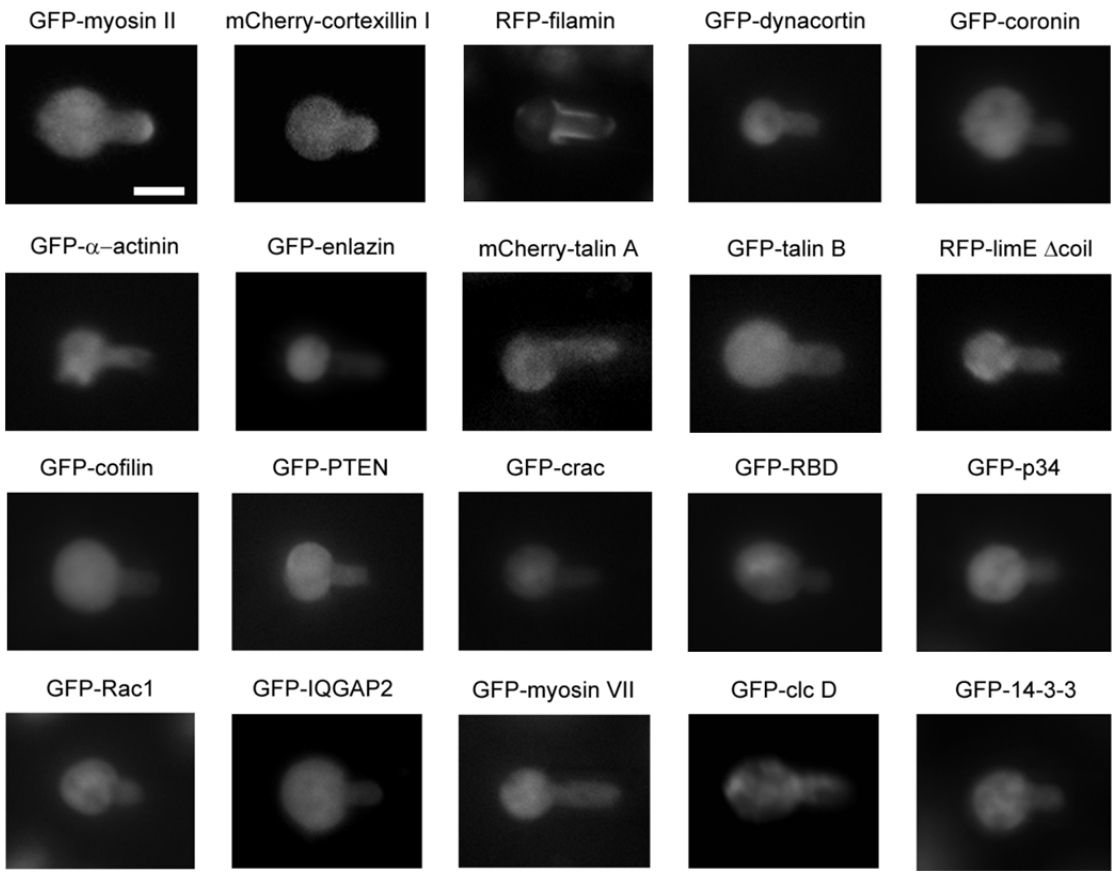

Supplementary Figure 9. The spatial distribution of different cytoskeletal proteins in *racE* null cells during micropipette aspiration. Scale bar, 10 μm.

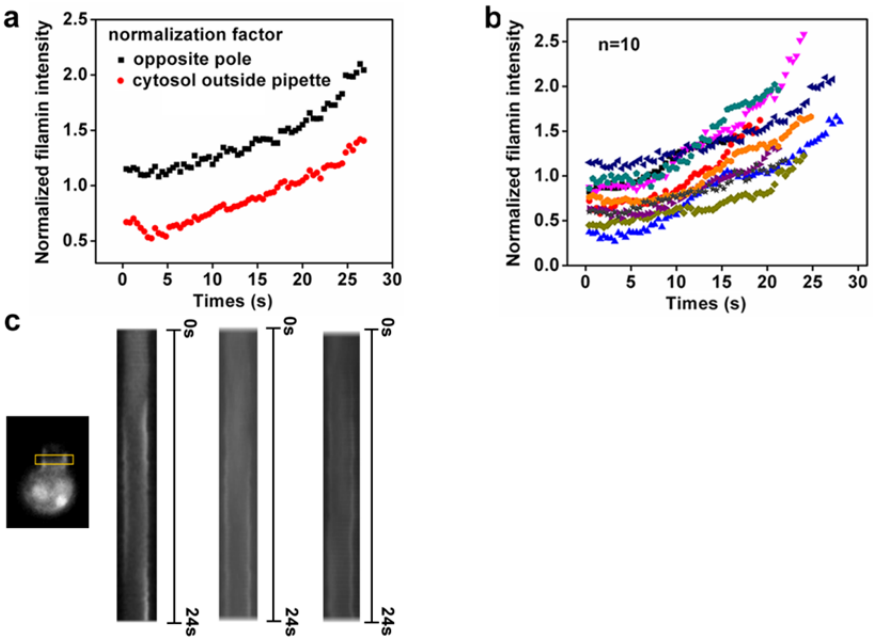

Supplementary Figure 10. The accumulation of filamin in *racE* null cells. **a**, The filamin intensity at the neck region normalized to the intensities at the opposite pole and the cytosol outside pipette show similar trends during accumulation although the absolute values are different. **b**, The kinetics of filamin accumulation in 10 different cells. **c**, The kymographs of filamin accumulation in the neck region in three different cells. The yellow box indicates the region where the signals were extracted.

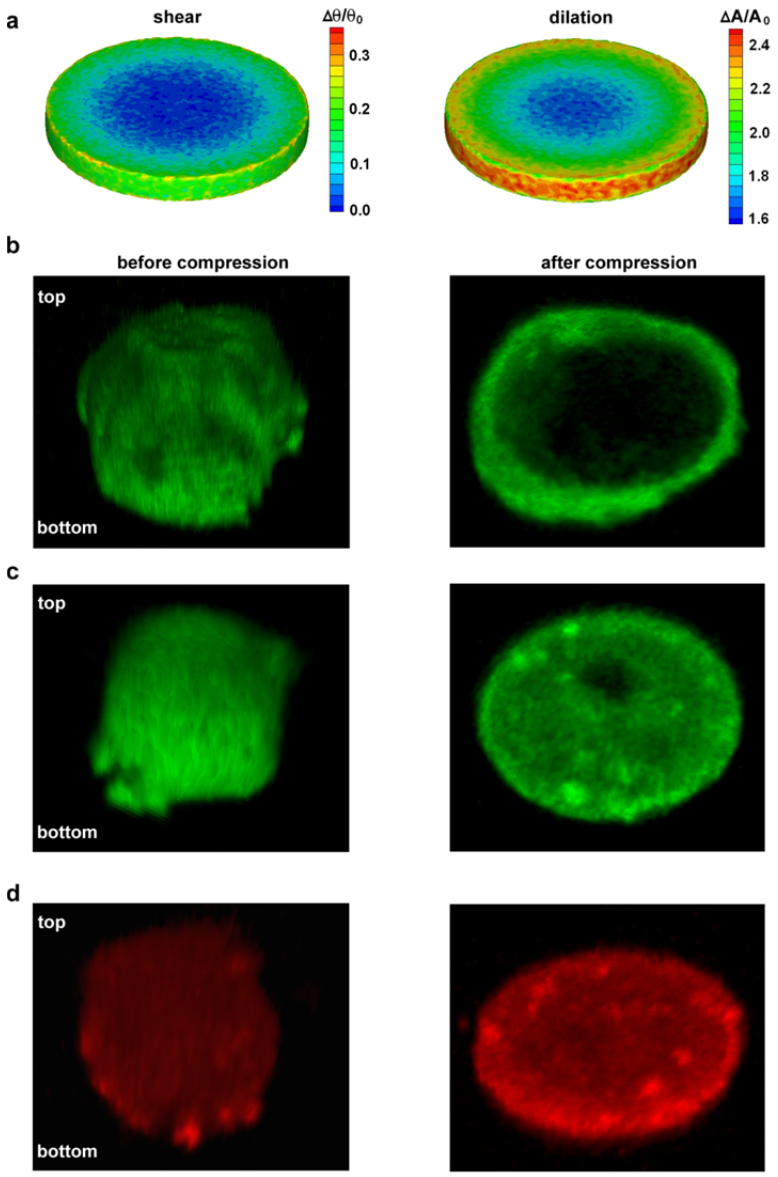

Supplementary Figure 11. Mechanosensitive accumulation of proteins in a compression assay. a, Simulated shear and dilation deformations for cells being compressed to a height of ~2μm (**Supplementary Text**). Both deformations have the highest values on the lateral surfaces. But, dilation deformation has a sharper gradient than shear deformation near the lateral surfaces. 3D-reconstructed confocal images for GFP-myosin II in WT cells, GFP-α-actinin in *myosin* II null cells, and RFP-filamin in *racE* null cells before and after compression are shown in **b**, **c** and **d** respectively. Due to the sharper gradient of dilation deformation than shear deformation, myosin II shows more significant accumulation than filamin along the lateral edges. In comparison, relative faster accumulations of α-actinin and filamin (~10 s) make it challenging to capture the strong accumulations of these proteins in the compression assay combined with confocal imaging.

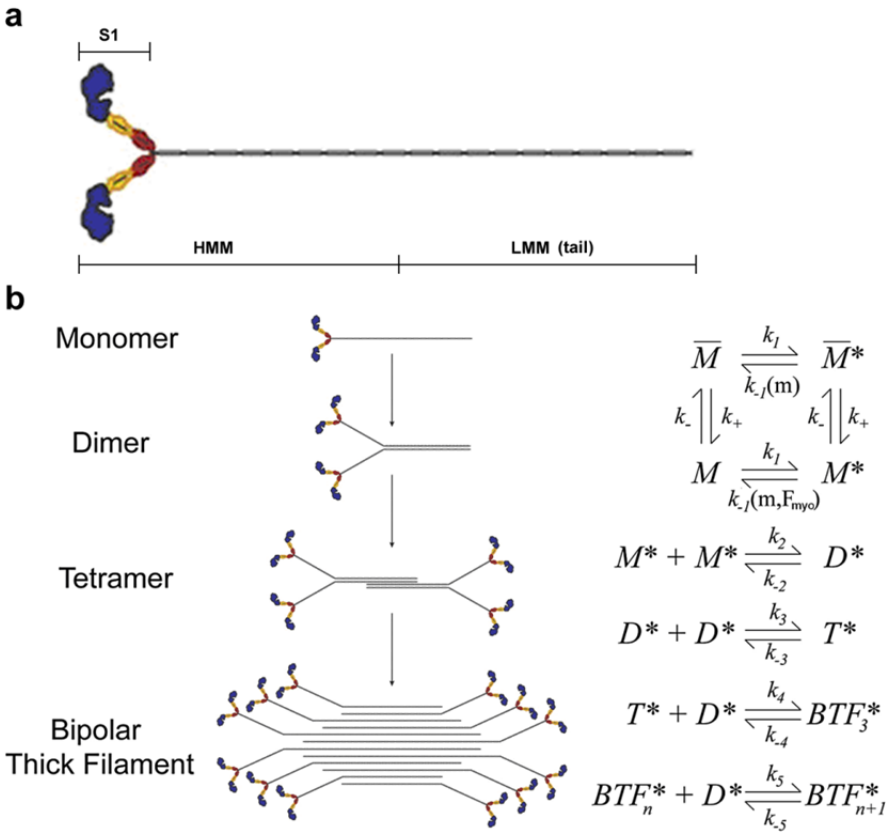

Supplementary Figure 12. The molecular structure of myosin II and its bipolar thick filament assembly scheme. a, The schematic graph of a myosin II monomer. **b**, The assembly scheme of a myosin II bipolar thick filament (adapted from Ref.[25]).

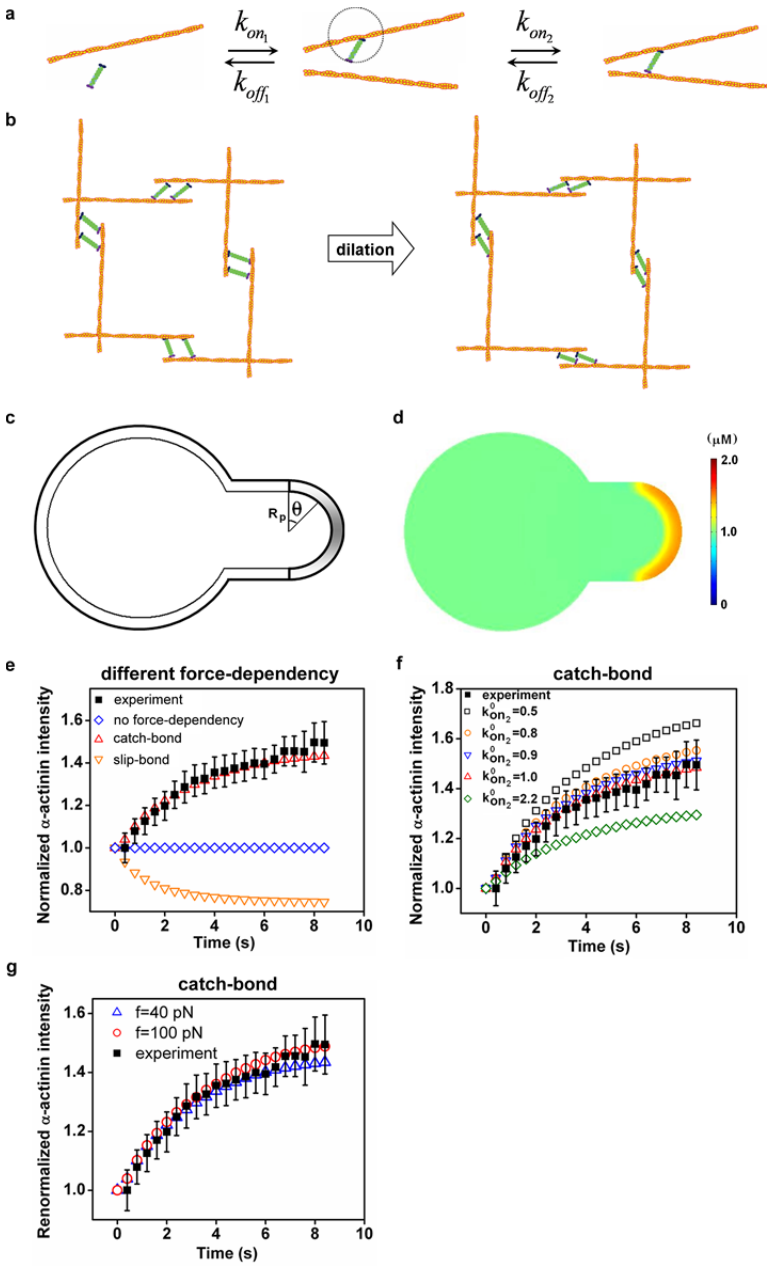

Supplementary Figure 13. The simulations of the accumulation of α-actinin in *myosin II* null cells with catch-bond or slip-bond models. **a**, The two-step force-dependent binding model of α-actinin to F-actin. **b**, The schematic graph of the dilation-induced deformation of bound α-actinin. Green structures represent the α-actinin dimers. **c**, The geometry used in the 3D simulation of α-actinin accumulation. The input force-profile is $f_{\max} \sin\theta$ where θ is the azimuth angle in the tip region, and $f_{\max}$ is 40 pN. The force is zero in other places. **d**, An example of simulated α-actinin accumulation at 8 s for the case of catch-bond model with k_{on_2} = 1.1 $\mu M^{-1}s^{-1}$. **e**, Comparison of simulation results using different models to experimental observations suggests that the catch-bond model captures the essential characteristics of the α-actinin behaviors. **f**, Sensitivity analysis of k_{on_2} for catch-bond model. **g**, Simulations with different forces $f_{\max}$ suggest that force does not have a dramatic effect on α-actinin when a catch-bond mechanism is used. **Supplementary Table 2** provides the other parameters.

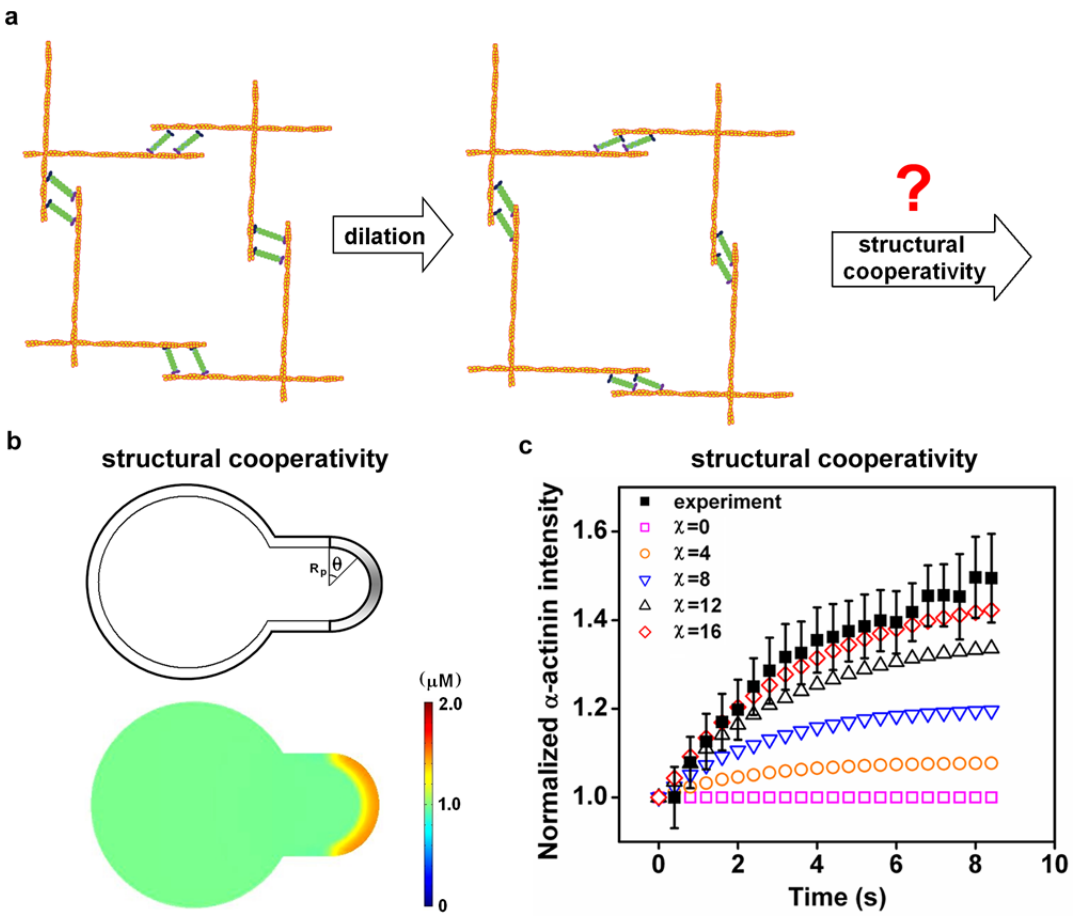

Supplementary Figure 14. Simulations of the accumulation of α-actinin in *myosin II* null cells based on structural cooperativity independent of force-dependent bond models. a, The schematic graph of the dilation-induced deformation of bound α-actinin and consequently leading to structural cooperativity which favors more α-actinin binding by increasing the on-rate. However, exactly how dilation induces the structural cooperativity at a molecular level remains unclear. **b**, The top panel shows the input cooperativity-profile $\chi \sin\theta$ where θ is the azimuth angle in the tip region. The on-rate in the second binding step is $k_{on_2} = k_{on_2}^0 \left(1 + [CrF_1F_2]/[F_2]\right)^{\chi \sin\theta}$. The bottom is one example of the simulated accumulation pattern for α-actinin at 8 s with the cooperativity index χ =16. **c**, Simulated α-actinin accumulations for various χ. For structural cooperativity model, **Supplementary Table 2** provides the other parameters.

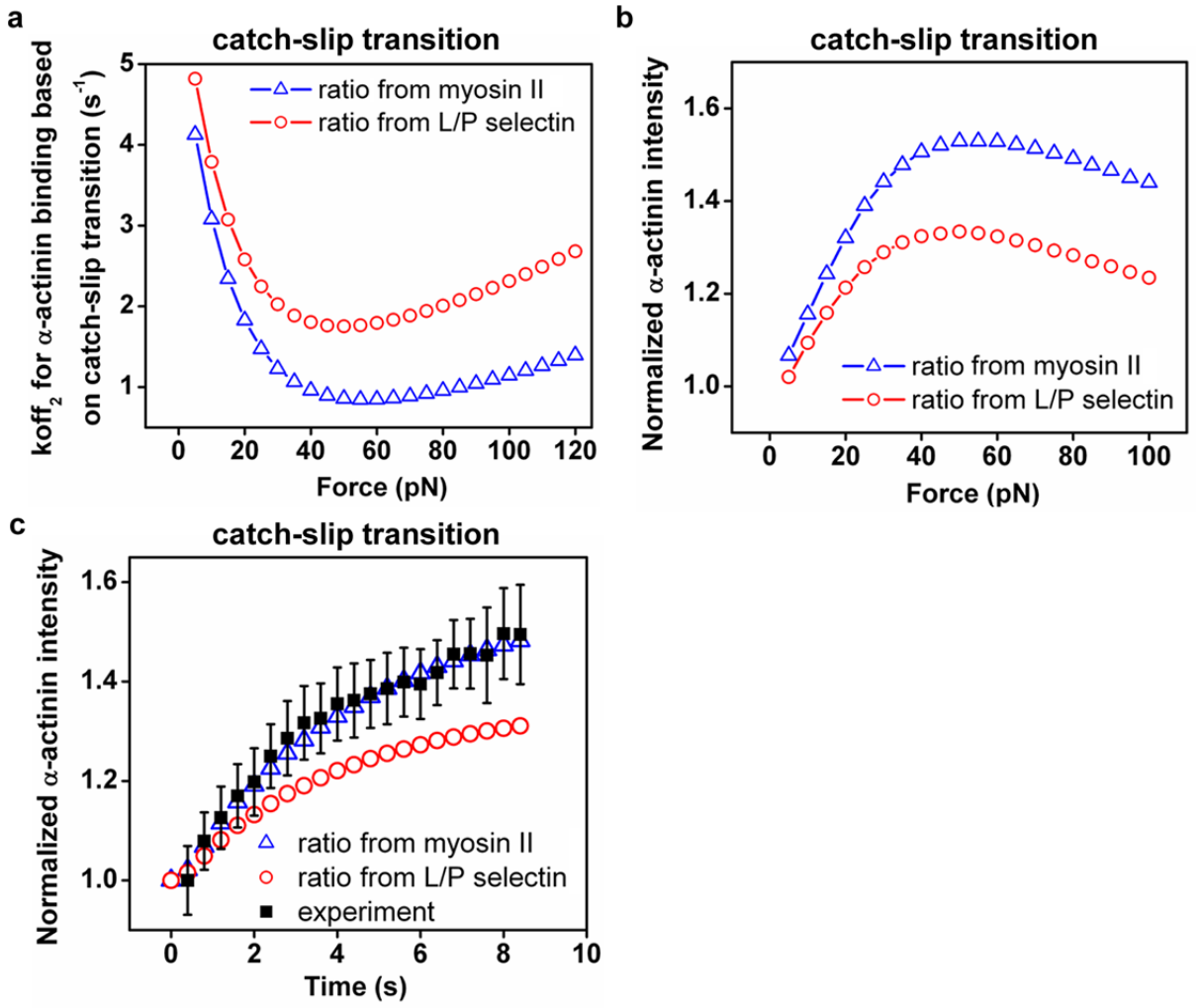

Supplementary Figure 15. The simulations of the accumulation of α-actinin in *myosin II* null cells based on catch-slip transition model. **a,** Plot shows the off-rate k_{off_2} as a function of force. $k_{off_2}^{c0}$ and Δx_c had the values measured experimentally [14, 34]. The values of $k_{off_2}^{s0}$ and Δx_s were calculated from the ratios of $k_{off_2}^{s0}/k_{off_2}^{c0}$ and $\Delta x_s/\Delta x_c$ used for muscle myosin II [28] and L/P selectin [27]. **b**, Simulated accumulations of α-actinin for 0-100 pN force displayed a rise-fall transition. **c**, The comparison between simulations and experiments suggests that the parameters derived from the ratio used for muscle myosin II accounts for α-actinin accumulation better than the ratios derived from L/P selectin**.** **Supplementary Table 2** provides the parameters for catch-slip transition model.

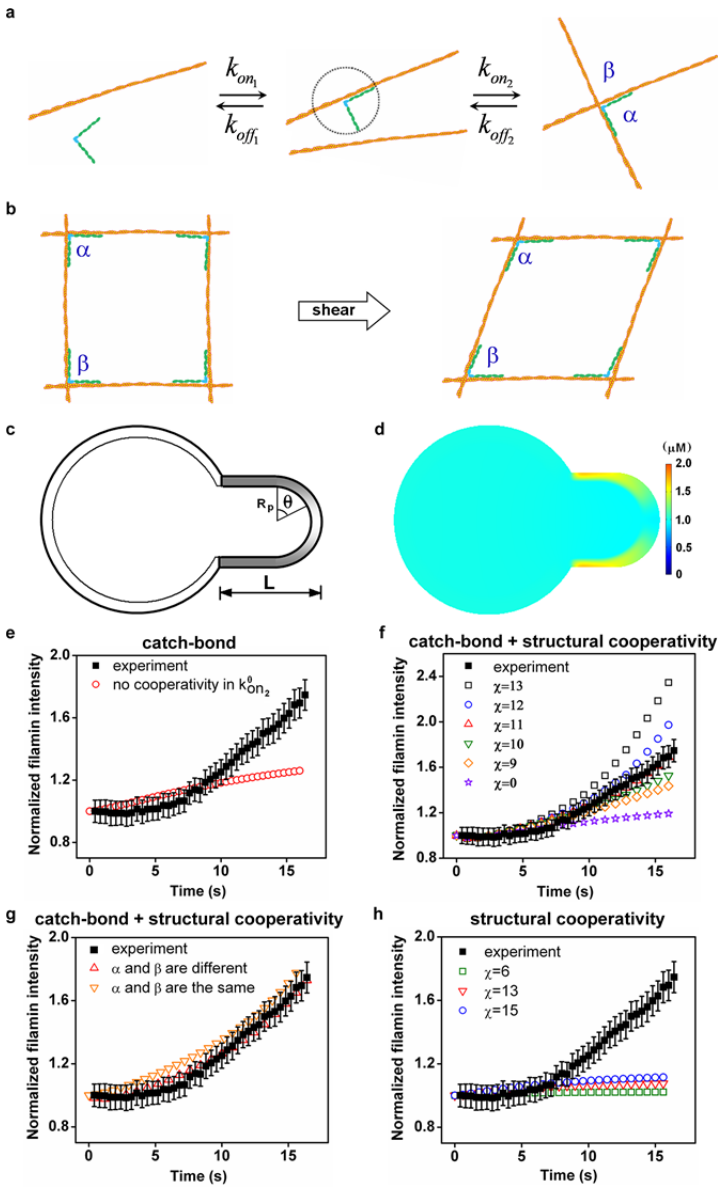

Supplementary Figure 16. The simulations of the accumulation of filamin (in *racE* null and dyn-hp cells) with the implementations of catch-bond model and structural cooperativity. **a**, The two-step force-dependent binding model of filamin to F-actin. **b**, The schematic graph of the shear-induced deformation of bound filamin. Green structures represent the filamin dimers. **c**, The geometry used in the 3D simulation of filamin accumulation. For catch-bond simulations, the input force-profile in the actin cortex is $f_{\max}\cos\theta$ where θ is the azimuth angle in the spherical tip region and $f_{\max}$ in the whole neck region. Here, $f_{\max}$ is 60 pN. The force is zero in other places. **d**, An example of simulated filamin accumulation at 12 s for the case of χ=11 and $k^0_{on_2}$ =0.01μM^{-1}s^{-1}. The remaining parameter values may be found in **Supplementary Table 3**. **e**, The sensitivity analysis of χ when $k^0_{on_2}$ =0.01μM^{-1}s^{-1}. **f**, Sensitivity analysis of $k^0_{on_2}$ when χ =11. **g**, Treating filamin proteins at α and β sites differently produces better simulation results as compared to the experiments. **h**, Simulations with structural cooperativity alone do not capture the kinetics of accumulation observed experimentally. The parameter values may be found in **Supplementary Table 3**.

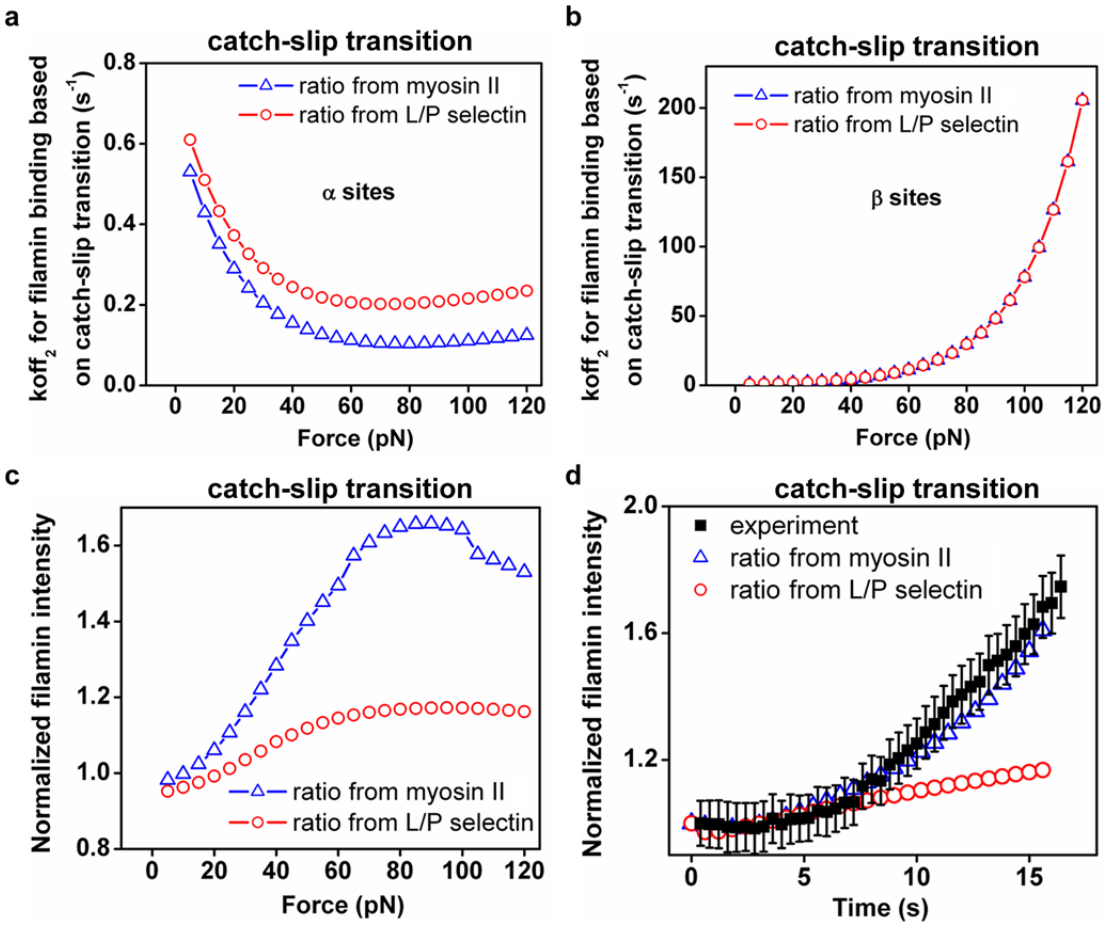

Supplementary Figure 17. The simulations of filamin accumulation in *racE* null cells based on the catch-slip transition model. a, b, The off-rates k_{off_2} for α and β sites as functions of force are presented. Values of $k_{off_2}^{c0}$ and Δx_c have been experimentally measured [14]. The values of $k_{off_2}^{s0}$ and Δx_s were calculated from the ratios of $k_{off_2}^{s0}/k_{off_2}^{c0}$ and $\Delta x_s/\Delta x_c$ used for muscle myosin II [28] and L/P selectin [27]. **c,** Simulated accumulations of filamin with 0-120 pN force displayed a rise-fall transition. **d,** The comparison between simulations and experiments suggests that the parameters derived from the ratio measured for muscle myosin II more readily accounts for filamin accumulation than those derived from L/P selectin**. Supplementary Table 3** provides the parameters for catch-slip transition model.

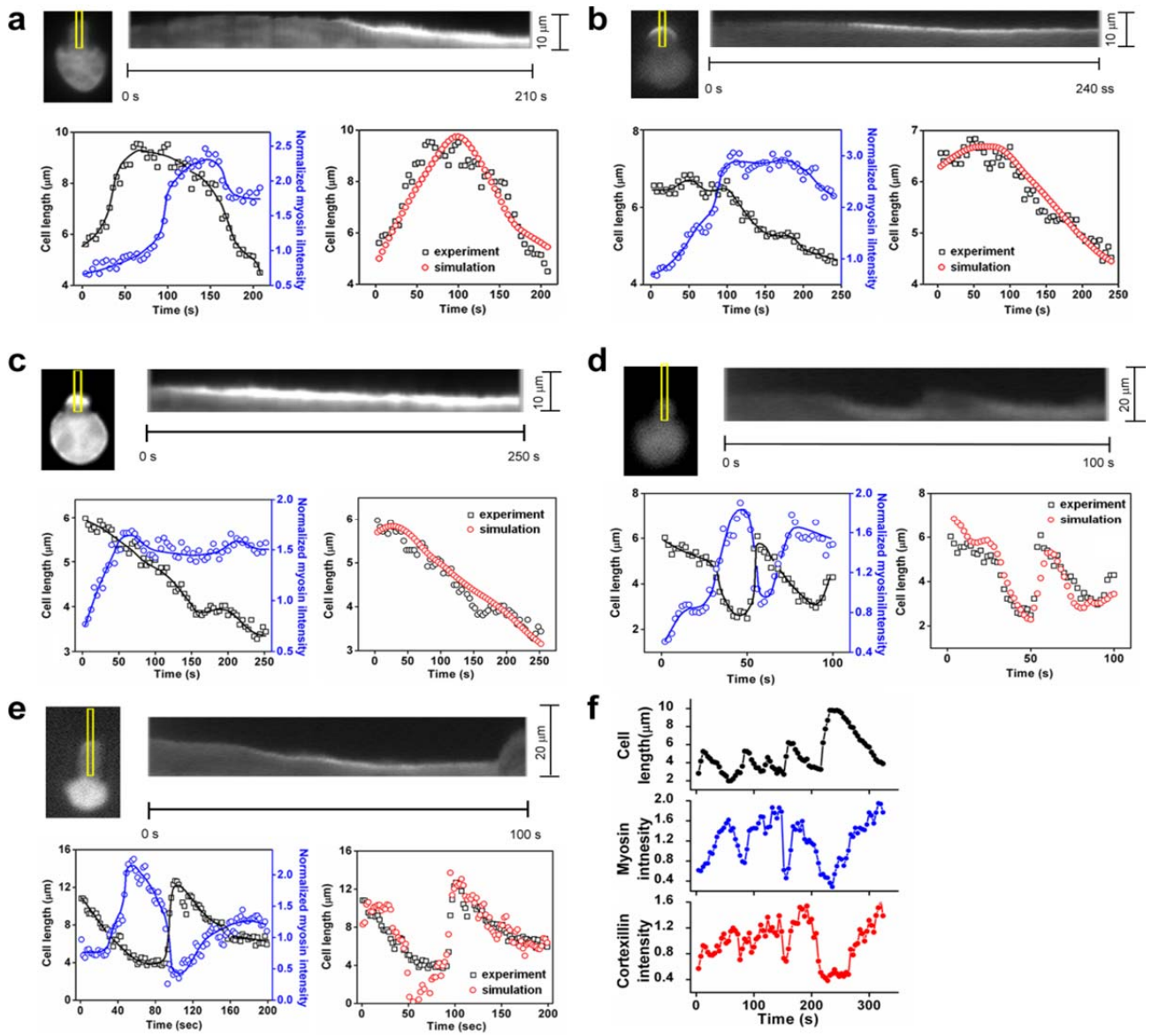

Supplementary Figure 18. Additional examples of the retraction of cells due to the accumulation of cytoskeletal proteins. **a**, The retraction of an *α-actinin* null cell. **b**, and **c**, are the retractions of *dynacortin-hp* cells. Panels **d**, and **e**, show examples of retractions of *racE* null cells. The upper panels of **a**, **b**, **c**, **d**, and **e**, are kymographs. The cell length (empty squares) and myosin II intensity (empty circles) were quantified and displayed in the lower left panels. The lower right panels show the comparison between the experimentally observed cell length and the one calculated from the viscoelastic model using the measured myosin II intensity as the input (**Supplementary Text**). **f**, The cell length measured in a *racE* null cell is negatively correlated with myosin II and cortexillin I intensities. **Supplementary Tables 4 and 5** provide the other parameters.

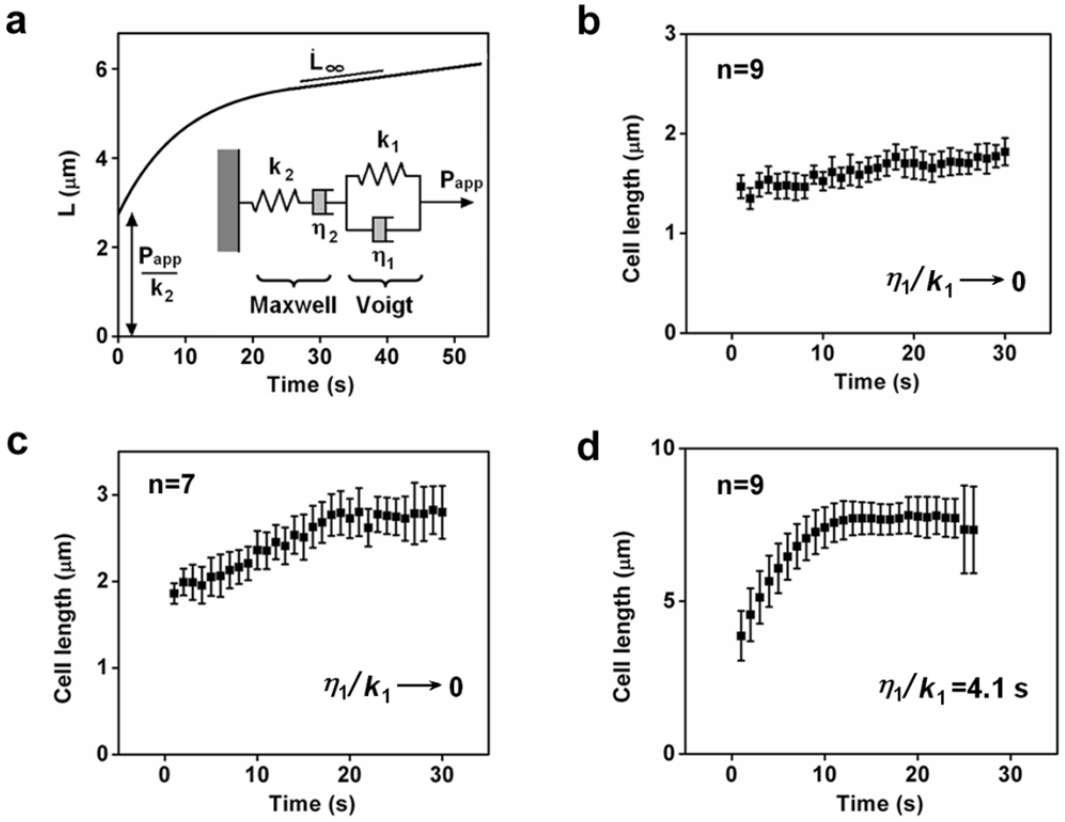

Supplementary Figure 19. The viscoelasticity of *Dictyostelium* cells. **a**, A schematic graph of creep test of a viscoelastic cell. The insert shows organization of the elastic and viscous components in this model. The initial transition has a characteristic time, $\tau = \eta_1/k_1$. When $\tau = \eta_1/k_1 \rightarrow 0$, the transition disappears. Panels **b**, **c**, and **d**, show the creep tests of *filamin* null, *α-actinin* null and *racE* null cells, respectively. The micropipettes had a diameter of 4 μm. The pressures were 0.5 nN/μm^2 for *filamin* null and *α-actinin* null cells and 0.15 nN/μm^2 for *racE* null cells. Extracted values of viscoelastic parameters are listed in **Supplementary Table 4**.

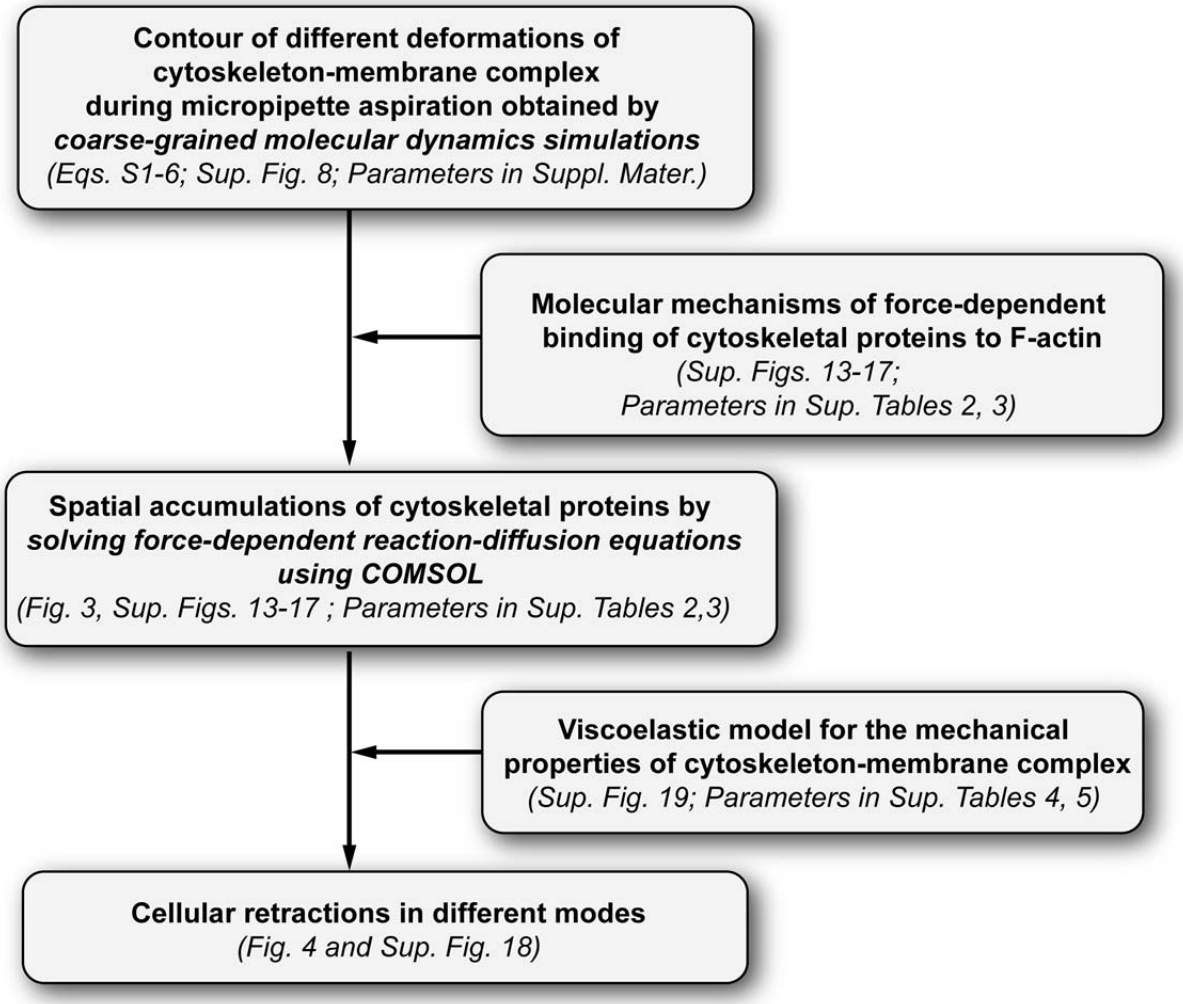

Supplementary Figure 20. The flow chart of the multi-scale simulations, including references to the figures and tables.

Supplementary Movie Descriptions

Movie S1. Myosin II accumulation in a WT cell during micropipette aspiration. Movies collected at 4 seconds between frames. Movies played at 2 frames/s.

Movie S2. The dynamics of fluorescent labeled actin in WT cells during micropipette aspiration. Movies collected at 0.4 seconds between frames. Movies played at 2 frames/s.

Movie S3. The dynamics of fluorescent labeled Lifeact in WT cells during micropipette aspiration. Movies collected at 0.8 seconds between frames. Movies played at 2 frames/s.

Movie S4. α-actinin accumulation in a *myosin II* null cell during micropipette aspiration. Movies collected at 0.4 seconds between frames. Movies played at 2 frames/s.

Movie S5. Filamin accumulation in a *racE* null cell during micropipette aspiration. Movies collected at 0.4 seconds between frames. Movies played at 2 frames/s.

Movie S6. Simulation result of myosin II accumulation in a WT cell during micropipette aspiration.

Movie S7. Simulation result of α-actinin accumulation in a *myosin II* null cell during micropipette aspiration.

Movie S8. Simulation result of filamin accumulation in a *racE* null cell during micropipette aspiration.

Movie S9. Oscillations of a *racE* null cell due to myosin II accumulation during micropipette aspiration. Movies collected at 1.5 seconds between frames. Movies played at 2 frames/s.